

# Epidemic models characterize seizure propagation and the effects of epilepsy surgery in individualized brain networks based on MEG and invasive EEG recordings

Ana. P. Millán<sup>1,\*</sup>, Elisabeth C.W. van Straaten<sup>1</sup>, Cornelis J. Stam<sup>1</sup>, Ida A. Nissen<sup>1</sup>, Sander Idema<sup>2</sup>, Johannes C. Baayen<sup>2</sup>, Piet Van Mieghem<sup>3</sup>, and Arjan Hillebrand<sup>1</sup>

<sup>1</sup>Department of Clinical Neurophysiology and MEG Center, Amsterdam Neuroscience, Vrije Universiteit Amsterdam, Amsterdam UMC, Amsterdam, The Netherlands

<sup>2</sup>Department of Neurosurgery, Amsterdam Neuroscience, Vrije Universiteit Amsterdam, Amsterdam UMC, Amsterdam, The Netherlands

<sup>3</sup>Faculty of Electrical Engineering, Mathematics and Computer Science, Delft University of Technology, Delft, The Netherlands

\*Corresponding author: [a.p.millanvidal@amsterdamumc.nl](mailto:a.p.millanvidal@amsterdamumc.nl)

## Abstract

### Background

Epilepsy surgery is the treatment of choice for drug-resistant epilepsy patients. However, seizure-freedom is currently achieved in only 2/3 of the patients after surgery. In this study we have developed an individualized computational model based on functional brain networks to explore seizure propagation and the efficacy of different virtual resections. Eventually, the goal is to obtain individualized models to optimize resection strategy and outcome.

### Methods

We have modelled seizure propagation as an epidemic process using the susceptible-infected (SI) model on individual functional networks derived from presurgical MEG. We included 10 patients who had received epilepsy surgery and for whom the surgery outcome at least one year after surgery was known. The model parameters were tuned in order to reproduce the patient-specific seizure propagation patterns as recorded with invasive EEG. We defined a personalized search algorithm that combined structural and dynamical information to find resections that maximally decreased seizure propagation for a given resection size. The optimal resection for each patient was defined as the smallest resection leading to at least a 90% reduction in seizure propagation.

### Results

The individualized model reproduced the basic aspects of seizure propagation for 9 out of 10 patients when using the resection area as the origin of epidemic spreading, and for 10 out of 10 patients with an alternative definition of the seed region. We found that, for 7 patients, the optimal resection was smaller than the resection area, and for 4 patients we also found that a resection smaller than the resection area could lead to a 100% decrease in propagation. Moreover, for two cases these alternative resections included nodes outside the resection area.

### Conclusion

Epidemic spreading models fitted with patient specific data can capture the fundamental aspects of clinically observed seizure propagation, and can be used to test virtual resections *in silico*. Combined with optimization algorithms, smaller or alternative resection strategies, that are individually targeted for each patient, can be determined with the ultimate goal to improve surgery outcome.

## 1 Introduction

Epilepsy is one of the most common neurological disorders, affecting between 4 and 10 per 1000 people worldwide [1]. There is not one single cause of epilepsy: it often occurs as an associated symptom of an underlying

43 disease, but many other times it is produced by unknown causes [2]. This complicates the understanding of  
44 seizure dynamics, and to this day the microscopic mechanisms that lead to seizure generation and propagation  
45 are not fully understood [3]. It is generally assumed that a shift from normal neuronal activity to excessive  
46 synchronization [4] occurs due to decreased inhibition [5], but the actual nature of this transition is not clear.

47 Epilepsy is initially treated by anti-epileptic drugs (AEDs), but this approach is not effective for roughly  
48 1 out of 3 people [6]. For these drug-resistant patients, epilepsy surgery is an optional treatment if a focal  
49 origin of the seizures can be found. The surgery then aims to remove or disconnect the brain regions thought  
50 to be involved in seizure generation. Currently, seizure freedom is achieved in up to 2 out of 3 patients who  
51 undergo epilepsy surgery, although surgery outcome varies greatly depending on epilepsy type [7]. Even when  
52 surgery is not completely successful, the majority of patients will still experience a reduction in seizure frequency  
53 or intensity after surgery. However, side-effects and cognitive complaints can also occur after surgery. These  
54 depend on the brain areas resected, but are difficult to predict accurately [8].

55 Traditionally, efforts to improve epilepsy surgery have aimed to better characterize the epileptogenic zone  
56 (EZ, defined as the minimal brain area or areas that need to be removed or disconnected to achieve seizure  
57 freedom [9]; by definition, this can only be confirmed after surgery, and prior to it only a hypothesis can be  
58 made). However, in recent years – and in line with the increasingly common view of the brain as a complex  
59 network – epilepsy is seen as a network disorder. Attention is thus shifting towards the definition of *epileptogenic*  
60 *networks* that can capture more details of seizure dynamics and the distribution of epileptiform activity [10–12].  
61 An increasing number of findings support this perspective: topological properties of epileptogenic brain networks  
62 have been found to deviate from those seen in healthy controls [13, 14], and abnormal patterns of functional  
63 connectivity emerge [15–17] (although the results of different imaging modalities are sometimes contradictory  
64 [15–20]). A common finding in pathological brain networks is the association of disease with network hubs [21,  
65 22]. In the case of epilepsy, hubs may facilitate the propagation of epileptiform activity to the rest of the brain  
66 [23–25]. Moreover, several studies have pointed out the existence of *pathological hubs*: abnormal, hyperconnected  
67 regions in the vicinity of the epileptic focus, which may facilitate seizure propagation [25–27].

68 Importantly, the network perspective of epilepsy implies that the effect of a resection cannot be predicted  
69 directly from the location of the removed region alone [28]: local resections can have widespread effects, but at  
70 the same time might not prevent the epileptogenic network from forming a new EZ eventually [29]. Computer  
71 models are then necessary to help predict the effect of a given resection [30]. Integrating patient specific data of  
72 different modalities, computer models allow us to test different resections *in silico* – i.e. using virtual resections –  
73 together with different markers of the EZ. Within this framework, Hebbink et al. [31] showed that the resection of  
74 the pathological network node is not necessarily the best approach to alleviate seizures, whereas Lopes et al. [32]  
75 found that the fraction of resected rich-club nodes correlated with surgery outcome. Going beyond topological  
76 network analysis, the simulation of ictal activity on top of brain networks can aid the identification of the EZ  
77 and prediction of surgery outcome, as well as predict possible side-effects. Such computational models can be  
78 used to identify epileptogenic areas [33, 34] or analyze different resection strategies [26, 32, 35–38], such that  
79 patient-specific resection strategies, that may lead to a better outcome or fewer side-effects than the standard  
80 surgery, can be tested [33, 39–41]. Validation of the models is usually attempted by looking for differences in the  
81 model predictions between seizure free and non-seizure free patients [42, 43] or by correlating seizure propagation  
82 on the model with the empirical data [44].

83 A basic consideration in the model definition is thus the nature of the underlying network. The temporal  
84 and spatial resolution of the resulting network-based model, and the interpretation of the connections between  
85 regions, will depend on the modality that was used to define the network structure. Studies on epileptogenic  
86 networks have considered both functional [32, 35, 37, 42, 43, 45] and structural [33, 36, 40, 41] networks, as they  
87 are both affected in patients with epilepsy [40–43]. However, functional networks can capture abnormalities in  
88 brain activity even in the absence of structural abnormalities [46]. Functional networks based on intracranial  
89 recordings [32, 35, 37, 42, 43] usually include ictal data and allow for highly precise characterization of some brain  
90 areas, however spatial sampling is sparse and biased due to an a priori hypothesis of the EZ, which may lead to  
91 bias in the analysis. Moreover, these invasive recordings are not always part of the presurgical evaluation. Non-  
92 invasive methods, such as Electro- and Magneto-Encephalography (EEG/MEG) have no risks of complications  
93 [47]. MEG is less affected by the skull and other tissue in the head, is reference-free and has higher spatial  
94 resolution than clinical scalp EEG [48]. This allows for a more accurate estimation of functional interactions  
95 between brain regions, and thus a more accurate reconstruction of the functional networks. MEG interictal  
96 resting-state functional brain networks have been used previously to identify the EZ [11, 27].

97 In general, most of the studies cited above made use of highly detailed non-linear models, such as neural mass  
98 models or theta models [49]. These models depend on several parameters that need to be adjusted beforehand,  
99 which complicates the optimization of the model and makes it difficult to obtain conclusions that are gener-  
100 alizable. As it is usually the case, an interplay exists between the generalizability and accuracy of the model,

101 such that optimizing the predictive power of a model often means reducing the number of tunable parameters  
102 [50]. Thus, simpler models with few parameters might prove more reproducible, especially if the behavior of  
103 the model is understood mathematically. In this regard, one particular framework of relative mathematical  
104 simplicity that may capture the fundamental aspects of seizure propagation is that of epidemic spreading models  
105 [51]. These models simulate the propagation of an agent from some given location to other connected areas, a  
106 basic phenomenon appearing in a multitude of systems. Such models have been used, for instance, to study the  
107 spreading of pathological proteins on brain networks [52], or the relation between brain structure and function  
108 [53].

109 We propose that epidemic models can also provide a good representation of the initial steps of seizure  
110 propagation, during which the anomalous highly synchronized ictal activity propagates from the EZ to other  
111 regions. Moreover, as it is the case in epilepsy surgery, studies on epidemic models often try to find ways to  
112 stop or limit the propagation of the epidemics. Thus, epidemic models could also aid the planning of epilepsy  
113 surgery. For instance, the fundamental role of hubs in propagation is a well-known result of epidemic spreading  
114 [54], and targeting hub regions is often the most efficient way to obtain global immunization [55, 56]. Data of  
115 outbreak patterns can also be used retroactively to find the location of the origin of an epidemic [57, 58]. Within  
116 this framework, in a previous study [41] we modelled seizure propagation as an epidemic spreading process and,  
117 using the eigenvector centrality as a surrogate measure, found that the size of the resection area could be largely  
118 reduced with only a small decrease in the efficacy of the virtual surgery.

119 Here we defined an individualized seizure propagation model by making use of the Susceptible-Infectious  
120 (SI) model of epidemic spreading on top of a global brain network, for a group of 10 epilepsy patients who  
121 underwent epilepsy surgery, and for whom the surgical outcome at least one year after surgery was known. The  
122 network was based on the patient-specific MEG functional connectivity. The model parameters were tuned using  
123 information about the patient-specific seizure propagation patterns in invasive EEG recordings and the location  
124 of the resection area. First, we showed that, despite its simplicity, the model provides a good approximation  
125 to clinically observed seizure propagation patterns, and we fit the free parameters of the model to optimize the  
126 reproduction of the individual seizures. Secondly, we used the individualized model to test alternative resection  
127 strategies and, making use of an optimization algorithm, we found optimal – in terms of reduction of seizure  
128 propagation – personalized resections.

## 129 2 Methods

### 130 2.1 Patient group

131 We retrospectively analyzed 10 patients (5 females) with refractory epilepsy (Table 1). All patients underwent  
132 epilepsy surgery at the Amsterdam University Medical Center, location VUmc, between 2016 and 2019. All  
133 patients had received a magnetoencephalography (MEG) recording, had undergone a SEEG (stereo-electro-  
134 encephalography) study, and underwent pre- and post-surgical MR imaging. All patients gave written informed  
135 consent and the study was performed in accordance with the Declaration of Helsinki and approved by the VUmc  
136 Medical Ethics Committee.

137 The patient group was heterogeneous with temporal and extratemporal resection locations and different  
138 etiology. Surgical outcome was classified according to the Engel classification at least one year after the operation  
139 [59]. Patients with Engel class 1A were labelled as seizure free (SF), and patients with any other class were  
140 labelled as non seizure free (NSF). 3 patients were deemed NSF.

### 141 2.2 Individualized Brain Networks

142 The individualized computer model was based on the functional brain network of each patient (see figure 1),  
143 which was reconstructed in the Brainnetome Atlas (BNA) from MEG scans, as detailed below. Pre-operative  
144 Magnetic resonance imaging (MRI) scans were used for co-registration with the MEG data. MRI T1 scans were  
145 acquired on a 3T whole-body MR scanner (Discovery MR750, GE Healthcare, Milwaukee, Wisconsin, USA) using  
146 an eight-channel phased-array head coil. Anatomical 3D T1-weighted images were obtained with a fast spoiled  
147 gradient-recalled echo sequence. During reconstruction, images were interpolated to 1mm isotropic resolution.

#### 148 2.2.1 MEG acquisition

149 MEG recordings were obtained during routine clinical practice using a whole-head MEG system (Elekta Neu-  
150 romag Oy, Helsinki, Finland) with 306 channels consisting on 102 magnetometers and 204 gradiometers. The  
151 patients were in supine position inside a magnetically shielded room (Vacuumshmelze GmbH, Hanau, Germany).

Patient	Sex	Age at Ep. Onset (y)	Duration of Ep. at Surgery (y)	MRI radiologic diagnosis	Pathology	Resection Area	S <sub>RA</sub>	Engel Score	Surgery Outcome	#E	#ECP	N <sub>SR</sub>
P1	F	20 – 29	10 – 19	normal MRI	mMCD-2	R-TL	5	2A	NSF	9	99	40
P2	M	20 – 30	10 – 19	normal MRI	mMCD-2	L-T	5	1A	SF	12	106	30
P3	F	40 – 50	30 – 39	normal MRI	mMCD-2	L-F	4	2C	NSF	13	117	47
P4	F	30 – 40	0 – 9	Multiple cavernoma	cavernoma & surrounding mMCD-2	L-T	5	1A	SF	11	110	44
P5	M	50 – 60	20 – 29	Post-traumatic gliosis	reactive changes	L-F	6	1A	SF	12	124	40
P6	F	20 – 30	10 – 19	normal MRI	mMCD-2	L-P	4	1A	SF	10	104	37
P7	M	20 – 30	10 – 19	FCD	mMCD-u	R-TPL, PL, PL	3	1A	SF	12	102	38
P8	F	50 – 60	20 – 29	normal MRI	FCD-2A	LT-MA	6	3A	NSF	15	194	60
P9	M	30 – 39	10 – 19	MTS	hippocampal sclerosis	RT-MA	12	1A	SF	10	107	32
P10	M	20 – 29	10 – 19	FCD	inconclusive	LI	6	1A	SF	14	193	49

Table 1: Patient data. Ep. = Epilepsy, y = years, S<sub>RA</sub> = number of resected ROIs, #E = number of intracranial electrodes, #ECP = total number of electrode contact points, N<sub>SR</sub> = number of BNA ROIs sampled by the SEEG electrodes. F = female, M = male, R = right, L = left, F = frontal, T = temporal, P = Parietal, TL = lateral temporal, TPL = posterior lateral temporal, PI = posterior insula, PL = posterior parietal, FCD = focal cortical dysplasia, mMCD = mild Malformation of Cortical Development, mMCD-2 = mMCD type 2, mMCD-u = mMCD type unknown, FCD-2A = focal cortical dysplasia type 2A, SF = seizure free, NSF = not seizure free.



152 Typically, three data-sets of 10 to 15 minutes each containing eyes-closed resting-state recordings were acquired  
153 and used in the presurgical evaluation for the identification and localization of interictal epileptiform activity.  
154 Paradigms for the localization of eloquent cortex, such as voluntary movements and somatosensory stimulation  
155 [60], as well as a hyperventilation paradigm to provoke interictal epileptiform discharges, were also recorded but  
156 not analysed in this study. The data were sampled at 1250 Hz, and filtered with an anti-aliasing filter at 410 Hz  
157 and a high-pass filter of 0.1 Hz. The head's position relative to the MEG sensors was determined using the signals  
158 from four or five head-localization coils that were recorded continuously. The positions of the head-localization  
159 coils and the outline of the scalp (roughly 500 points) were measured with a 3D digitizer (Fastrak, Polhemus,  
160 Colchester, VT, USA), and were later used for co-registration with the anatomical MRI.

161 The temporal extension of Signal Space Separation (tSSS) [61, 62] was used to remove artifacts using Maxfilter  
162 software (Elekta Neuromag, Oy; version 2.1). The points on the scalp surface were used for co-registration with  
163 the anatomical MRI of the patient through surface-matching software. A single sphere was fitted to the outline  
164 of the scalp and used as a volume conductor model for the beamforming approach. For a detailed description  
165 and parameter settings see [60].

## 166 2.2.2 MEG processing: Atlas-based Beamforming

167 Neuronal activity was reconstructed using an atlas-based beamforming approach, modified from [63], in which  
168 the time-series of neuronal activation of the centroids of the ROIs were reconstructed [64]. We considered the  
169 246 ROIs in the BNA atlas [65], including 36 subcortical ROIs, whose centroids were inversely transformed to  
170 the co-registered MRI of the patient. Then, a scalar beamformer (Elekta Neuromag Oy; beamformer; version  
171 2.2.10) was applied to reconstruct each centroid's time-series. The beamformer weights were calculated for each  
172 centroid separately to form a spatial filter so as to maximally let pass signals that originate from the centroid  
173 of interest and to attenuate all other signals. The weights were based on the lead fields (using the spherical  
174 head model and an equivalent current dipole as source model), the data covariance and noise covariance. The  
175 broadband (0.5 – 48.0 Hz) data covariance was based on the entire recording (on average 799.23 seconds of data  
176 (range: 309.50 - 908.67) were used). A unity matrix was used as noise covariance when estimating the optimum  
177 source orientation for the beamformer weights [66]. The broadband data were projected through the normalised  
178 beamformer weights [67] in order to obtain time-series (virtual electrodes, VE) for each centroid [64].

## 179 2.2.3 Brain Functional Networks

180 The time-series for each VE were visually inspected for epileptiform activity and artifacts. On average, 53.1  
181 (range: 19 – 60) interictal and artefact-free epochs of 16384 samples were selected for each patient. The epochs  
182 were further analyzed in Brainwave (version 0.9.151.5 [69]) and were down-sampled to 312 Hz, both in the  
183 broadband (0.5 - 48 Hz) and in the alpha-band (8 - 13 Hz).

184 Functional networks were generated using the 246 VEs as nodes (see figure 1a). Functional connectivity  
185 (i.e. the elements  $w_{ij}$  of the weight matrices) was estimated by the AEC (Amplitude Envelop Correlation)  
186 [70–73]. The uncorrected AEC (i.e. without correcting for volume conduction) connectivity metric was selected  
187 as it maintains information on the structural connectivity pattern, whilst including information on long-range  
188 functional connections. AEC values range from 0 (no functional connectivity) to 1 [74]. Functional networks  
189 were thresholded at different levels  $\theta$  indicating the percentage of remaining links, and the resulting average  
190 connectivity  $\kappa = \theta N$  of the network was determined. We considered a non-uniform grid in  $\theta$ , with values  
191  $\theta = 0.01, 0.02, 0.04, \dots, 0.10, 0.15, \dots, 0.50$ , to account for the fact that the model is more sensitive to connectivity  
192 changes for small  $\theta$ . Notice that the networks were thresholded but not binerized, so that  $w_{ij}$  remains a real  
193 variable ( $w_{ij} \in [0, 1]$ ). The resulting weight matrix is represented in figure 1a for a characteristic case.

## 194 2.2.4 Resection Area

195 The resection area (RA) was determined for each patient from the three-month post-operative MRI. This was  
196 co-registered to the pre-operative MRI (used for the MEG co-registration) using FSL FLIRT (version 4.1.6)  
197 12 parameter affine transformation. The resection area was then visually identified and assigned to the corre-  
198 sponding BNA ROIs, name those that were overlapping for at least 50% with the resection area. In figure 1 we  
199 illustrate the resection area and its connectivity structure with the rest of the network for one patient.

## 200 2.3 Individualized Propagation Pattern

201 All patients underwent stereo-electroencephalography (SEEG) electrode implantation. The number and loca-  
202 tion of the intracerebral electrodes (Ad-Tech, Medical Instrument Corporation, USA, 10-15 contacts, 1.12 mm

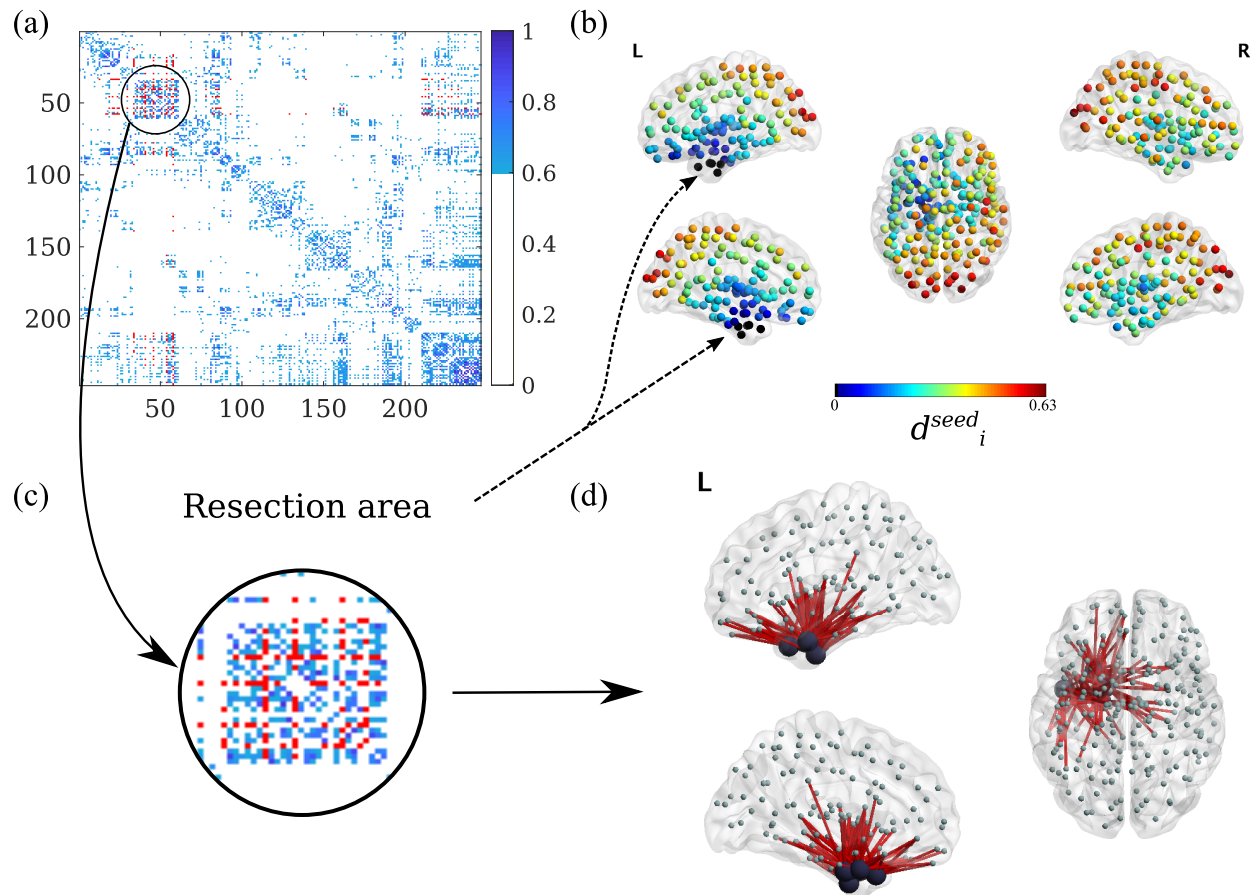
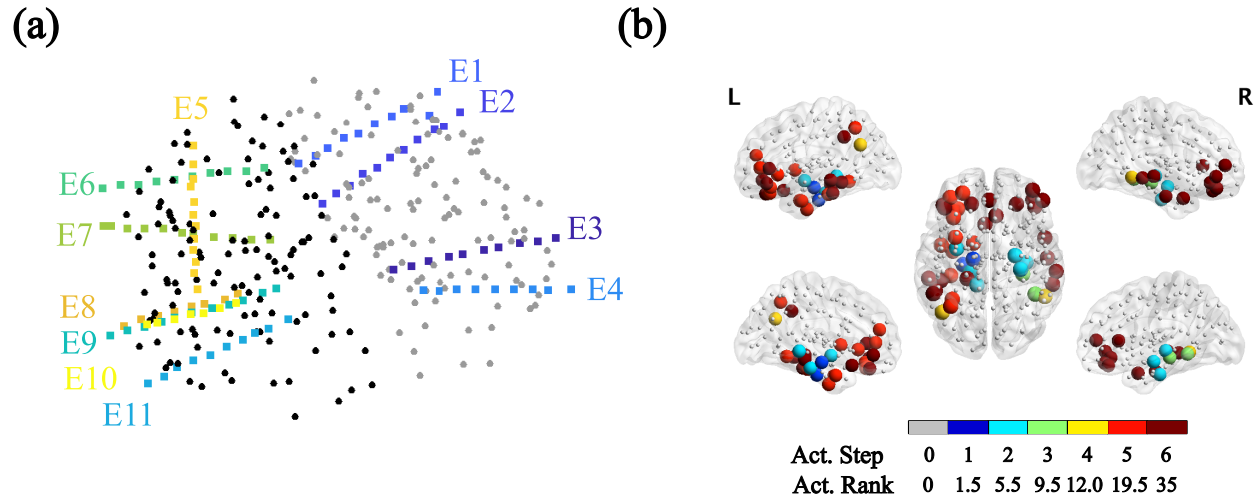


Figure 1: **Individual Brain Networks.** **a)** Weighted (and thresholded) resting-state broadband-MEG connectivity matrix for patient 4, for  $\theta = 0.15$ . Each entry corresponds to a BNA region, and the regions have been re-ordered to group regions in the same hemisphere. In this representation, ROIs 1-105 correspond to the left cortical regions, ROIs 106-210 to the right cortical regions and ROIs 211-246 to the subcortical regions (in alternating hemisphere order). The strength of each connection is indicated by the colorcode. In red we show the connections from and to the resection area (RA). **b)** Distribution of average distances to the RA according to eq.(S2) for patient 4, in dimensionless units. The points mark the centroids of the BNA ROIs, and the color scale indicates the effective distance of the ROI to the resection area (RA), which appears as black dots. **c)** Zoom-in of the adjacency matrix: RA and surrounding nodes. **d)** Illustrative representation of the RA (big black circles) and all the links connecting it with the rest of the network. Figures with brain representations have been obtained with the BrainNet Viewer [68].



**Figure 2: Individualized Seizure Propagation Pattern.** **a)** SEEG electrodes for patient 4. Black and gray dots indicate the BNA ROIs' mass centers, respectively for the left and right hemispheres (different colors are used for visualization purposes). This patient had 11 intracranial electrodes implanted, each electrode is shown in a different color. **b)** Corresponding seizure pattern constructed from the clinical SEEG recordings. First, different activation steps were identified in the seizure recordings, together with the corresponding contact points (CPs). In the case depicted here, typical seizures consisted of 6 propagation steps, with step 1 depicting the seizure onset zone (as indicated by the SEEG recordings), and step 6 signalling the generalization of the seizure to all sampled CPs (note however that in general not all CPs need take part in the seizure propagation pattern). This propagation pattern was then translated into the BNA space, and the sampled ROIs are indicated here as large colored spheres. Thus, only the BNA ROIs sampled by the SEEG electrodes are included in the pattern, which in this case corresponded to a total of  $N_{RS} = 49$  sampled ROIs ( $N_{RS}$  values for all patients are reported in table 1). The color code in the figure indicates the propagation step in which the corresponding CP is involved in ictal activity (i.e. Act. Step). Small grey dots mark the ROIs not included in the SEEG pattern. Finally, in order to enable comparison with the SEEG propagation pattern with the one modelled via the SI dynamics via the Mann-Whitney U test, we calculated the activation rank (Act. Rank) of each ROI, such that the ROIs were ordered and ranked according to the activation step, and groups with the same rank were assigned a rank equal to the midpoint of unadjusted values.

203 electrode diameter, 5 mm intercontact spacing; and DIXIE, 10-19 contacts, 0.8 mm electrode diameter, 2 mm  
204 contact length, 1.5 insulator length, 16 – 80.5 insulator spacer length) were planned individually for each patient  
205 by the clinical team, based on the location of the hypothesized seizure onset zone (SOZ) and seizure propagation  
206 pattern. Implantation was performed with a stereotactic procedure. The number of electrodes per patient varied  
207 between 9 and 15 (average = 11.8) and the total number of contacts between 99 and 194 (average = 125.6).  
208 Details of the number of electrodes and contact points for each patient are indicated in table 1.

209 The locations of the SEEG contact points were obtained from the post-implantation CT scan (containing  
210 the SEEG electrodes) that was co-registered to the preoperative MRI scan using FSL FLIRT (version 4.1.6) 12  
211 parameter affine transformation (see figure 2a). Each electrode contact point (CP) was assigned the location  
212 of the nearest ROI mass center. Because BNA ROIs are in general larger than the separation between contact  
213 points, different CPs can have the same assigned ROI. We refer to the set of ROIs sampled by the SEEG CPs  
214 as  $SEEG_{ROI}$ , with the size of the set being  $N_{SR}$  ( $N_{SR}$  values for all patients are reported in table 1).

215 Based on the clinical recordings, a seizure propagation pattern was built indicating the order of activation  
216 of the electrode CPs for a typical seizure, as shown in figure 2b. In order to do so, the start of ictal activity  
217 of typical seizures was visually assessed for each SEEG CP by a clinician expert. Then, the CPs were grouped  
218 into activation steps according to when ictal activity was first observed. The seizure pattern was built from one  
219 typical seizure for each patient. This activation pattern was then translated into the BNA space (see figure 2b),  
220 so that the each ROI  $i$  in the sampled set  $SEEG_{ROI}$  was assigned an activation step. Finally, we calculated the  
221 *activation rank* of each ROI in  $SEEG_{ROI}$ , such that the  $SEEG_{ROI}$  ROIs were ordered and ranked according to  
222 their activation step, and groups with the same rank (i.e. in the same activation step) were assigned a rank  
223 equal to the midpoint of unadjusted values (see figure 2b). This yields the SEEG pattern  $RANK_i^{SEEG}$  indicating  
224 the activation rank of each ROI  $i$  in  $SEEG_{ROI}$ .

## 2.4 Seizure Propagation Model

### 2.4.1 SI Dynamics

225  
226  
227 Seizure propagation was modelled via an epidemic spreading model: the susceptible-infected (SI) model [51].  
228 This model depicts the propagation of an epidemic process on a network from a set of seed regions to the rest  
229 of the nodes. The model only accounts for the propagation process, as it does not include any mechanisms  
230 for the deactivation of the affected regions. It thus represents the initial steps of the propagation of a seizure,  
231 before inhibition takes place and the affected regions start to deactivate. Thus, we do not try to mimic the  
232 complicated processes involved in seizure generation and propagation with this model, which is used here as an  
233 abstraction that includes only the most relevant features of the initial steps of seizure propagation. Thanks to  
234 its simplicity, the model can be described by using only one parameter, the infection probability  $\beta$ , as described  
235 below. More complicated epidemic models, such as the SIR or SIS model [51], which include a deactivation  
236 mechanism, introduce more parameters that either have to be assumed or fitted with detailed data.

237 Simulation of the epidemics on the network takes place as follows. Each node is characterized by its state:  
238 either S (susceptible) or I (infected). Initially, all nodes are in the S state, except for a set of nodes in the I  
239 state, which act as the seed of the epidemic (or seizure). At each time step, each infected node can propagate  
240 the infection independently to any of its neighbours with probability  $\beta w_{ij}$ , where  $\beta$  characterizes the rate of the  
241 epidemic spreading and  $w_{ij}$  is the connection strength between nodes  $i$  and  $j$  as given by the MEG-FC adjacency  
242 matrix. The fraction of infected nodes at each time is given by  $I(t)$ . If all nodes are connected, eventually the  
243 epidemic spreads over the whole network,  $I(t \rightarrow \infty) = 1$ , as shown in figure 3a. However, the speed and pattern  
244 of the propagation depend on  $\beta$  and  $w_{ij}$  (see figure 3).

245 In order to fit and validate the model, we first considered the situation of slow propagation in which only one  
246 new node is infected at each time step (formally corresponding to  $\beta \rightarrow 0$ ), and compared the propagation pattern  
247 of the modelled epidemic process with the clinical SEEG seizure pattern for different connectivity thresholds  $\theta$ .  
248 The threshold was then fit to maximize the correlation between the modelled and clinical propagation patterns.  
249 Then, to study the effect of different virtual resections, we quantified the short-term propagation of the seizure  
250 as the fraction of infected nodes at time  $t_0$ . Here we set  $t_0 = 50$  and, in order to account for different network  
251 densities, we set  $\beta\theta = \text{const} = 4 \cdot 10^{-4}$  (so that  $\beta = 0.01$  for a network with 4% of the links, for instance). For a  
252 standard resection size  $S_{RA}$  of 4 nodes this would correspond, in the uniform limit, to an infection of about 2/3  
253 of the nodes [50].

254 SI dynamics was simulated in custom-made Matlab algorithms using Monte-Carlo methods, with  $N_R = 10^4$   
255 iterations of the algorithm for each configuration to assure convergence.

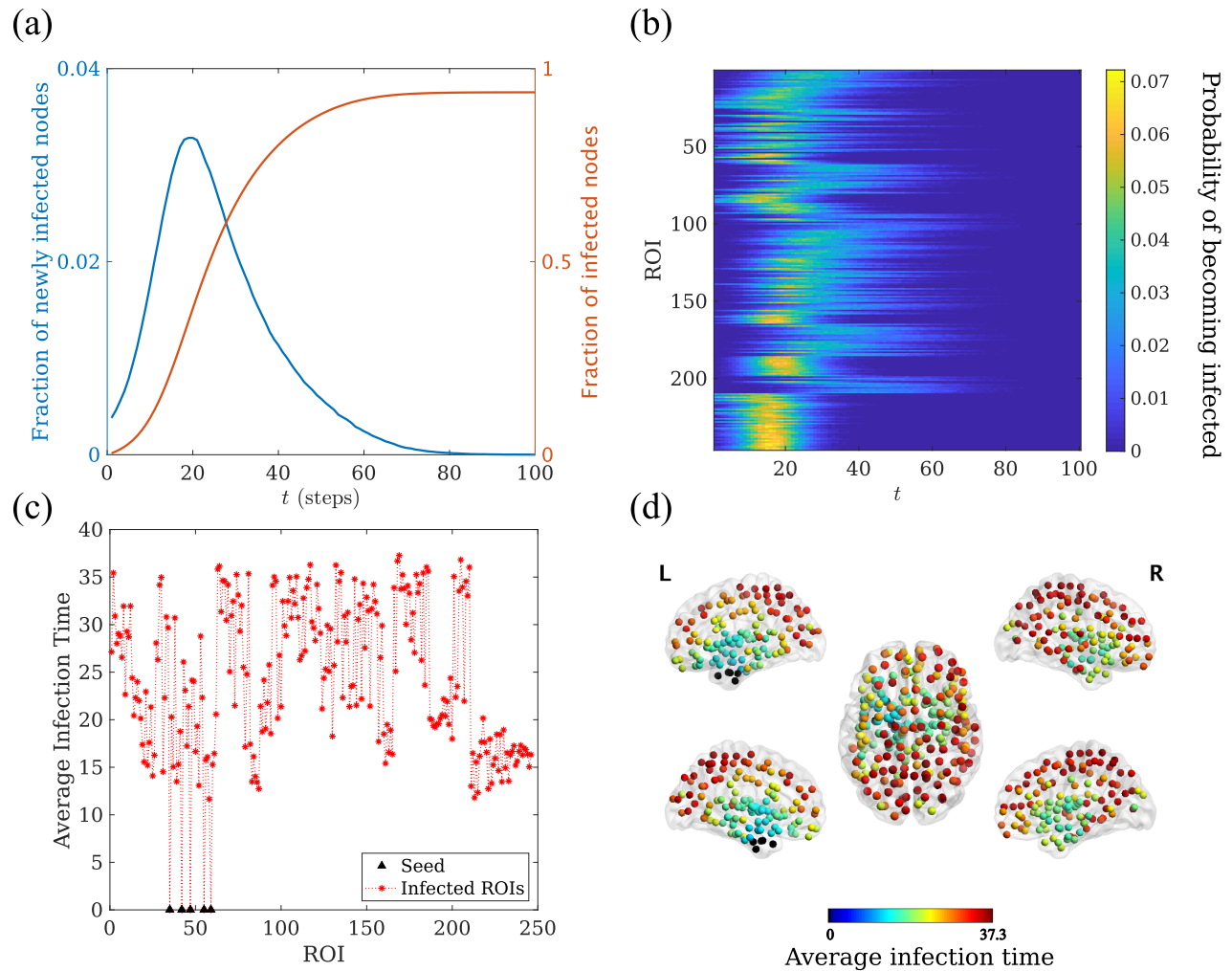


Figure 3: **Seizure propagation model.** Exemplary SI propagation process for patient 4. **(a)**  $I(t)$  (red line) and the fraction of newly infected nodes at time  $t$  ( $I(t) - I(t-1)$ , blue line), as functions of time. **(b)** Model propagation pattern showing the probability  $p_i(t)$ , as indicated by the color scale, that a given ROI  $i$  (y-axis) becomes infected at time  $t$  (x-axis). **(c)** Average infection time for each ROI,  $t_i$ . The seed (corresponding to the resection area, shown in black triangles) is always infected at time 0. **(d)** Spatial representation of the ROIs mean infection time  $t_i$ . Each ROI is color-coded according to its average infection time. The resection area is shown as black circles. The time unit is the number of simulation steps in all panels.

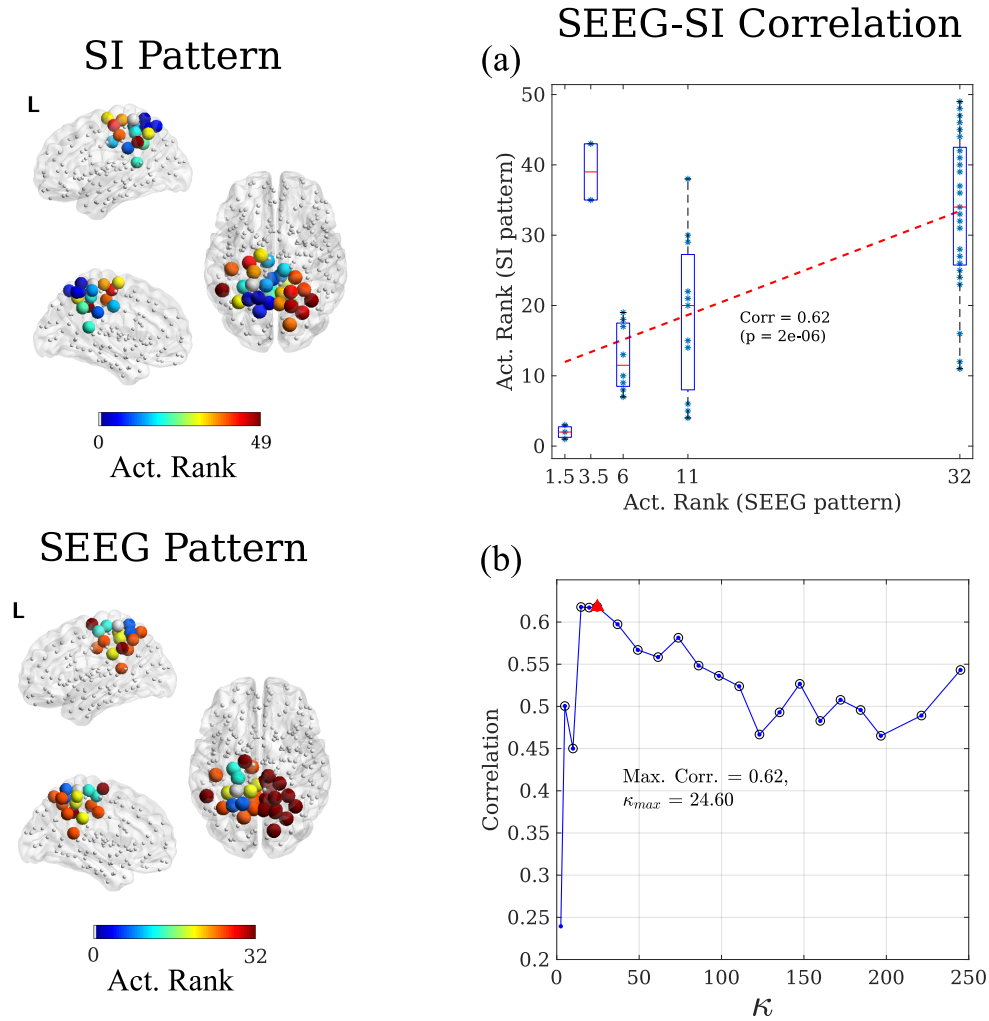


Figure 4: **Correlation method.** Here we illustrate, for patient 3, the correlation method to validate and fit the seizure propagation model. For each network connectivity threshold  $\theta$ , the SI dynamics was simulated over the whole MEG network, and the propagation pattern was constructed for the ROIs sampled by the SEEG electrodes and compared with the clinical SEEG pattern. Each pattern describes the activation order – or rank – of each sampled ROI. Given that the clinical SEEG pattern is built in term of activation steps, different ROIs can have the same ranking, as described in the main text. The modelled SI pattern was correlated with the clinical SEEG pattern, as depicted in panel (a). This process was iterated for different connectivity thresholds  $\theta$  leading the correlation curve shown in panel (b), where the mean degree  $\kappa = \theta N$  is shown in the x-axis, and significant correlations are indicated with a black circle. Finally, the connectivity leading to the maximum correlation was chosen. In the depicted case, this corresponded to a mean degree of  $\kappa = 24.60$  ( $\theta = 0.1$ ) leading a correlation of 0.62 (red triangle). This also corresponds to the value of  $\kappa$  used for panel a.



## 2.4.2 Optimization of SI parameters: Individualized Propagation Model

The SI dynamics were simulated as described above, leading to a probability map indicating the probability  $p_i(t)$  that each ROI  $i$  became infected at step  $t$ , for each connectivity threshold  $\theta$ , as shown in figure 3b. The mean activation time for each ROI was then calculated as  $t_i = \sum_{t=0}^T p_i(t)$ , where  $T$  is the maximum integration time.  $t_i$  describes the activation sequence of the ROIs during a modelled seizure (see figure 3c, d). Given that not all BNA ROIs were sampled by the SEEG electrodes,  $t_i$  was then sub-sampled to the  $\text{SEEG}_{\text{ROI}}$  set, and the included ROIs were ranked according to  $t_i$ . This ranking  $\text{RANK}_i^{\text{SI}}$  constitutes the modelled or SI seizure propagation pattern, which is defined upon the same set of ROIs  $\text{SEEG}_{\text{ROI}}$  as the clinical one ( $\text{RANK}_i^{\text{SEEG}}$ ), as shown in figure 4.

Once the SI pattern had been constructed, the ranked correlation was computed to compare the SI and SEEG patterns (see figure 4a) via a Mann-Whitney U test. The correlation is thus defined as

$$C = \frac{\text{cov}(\text{RANK}_i^{\text{SEEG}}, \text{RANK}_i^{\text{SI}})}{\sigma(\text{RANK}_i^{\text{SEEG}}) \sigma(\text{RANK}_i^{\text{SI}})} \quad (1)$$

where  $\text{cov}(x, y)$  and  $\sigma(x)$  respectively stand for the covariance and standard deviation. The connectivity threshold that maximized this correlation was independently found for each patient (see figure 4b) and used for the corresponding individualized virtual resection model.

Two possible seeds were considered for the SI dynamics: either the resection area (RA seed), or the hypothesized Seizure Onset Zone according to the SEEG clinical recordings (SOZ seed).

## 2.5 Simulation of Resections

Resections  $\mathcal{R}$  of sets of nodes were conducted in the model by the use of *virtual* resections (VRs). For this, all the connections of the corresponding nodes were set to 0, so the size of the network was left unchanged, but the resected nodes became isolated. Each resection  $\mathcal{R}$  was then characterized by measuring the fraction of infected nodes at a fixed time  $t_0$  after the resection had taken place,  $I_{\mathcal{R}}(t_0)$  (see figure 5).

The goal of epilepsy surgery is to completely stop seizure propagation ( $I_{\mathcal{R}}(t_0) \rightarrow 0 \forall t_0$ ) which, in the present model, can only be attained by (and it is always attained by [75, 76]) complete disconnection of the assumed seed region. Thus, in this study the effect of each resection was measured in terms of the decrease in the speed of seizure propagation, and the goal was to find the smallest resection able to reduce the initial propagation at  $t_0$  by 90%. That is, to find the smallest resection such that  $i_{\mathcal{R}} = I_{\mathcal{R}}(t_0)/I(t_0) \leq 0.1$ , where  $I(t_0)$  is measured on the original pre-resection network [41].

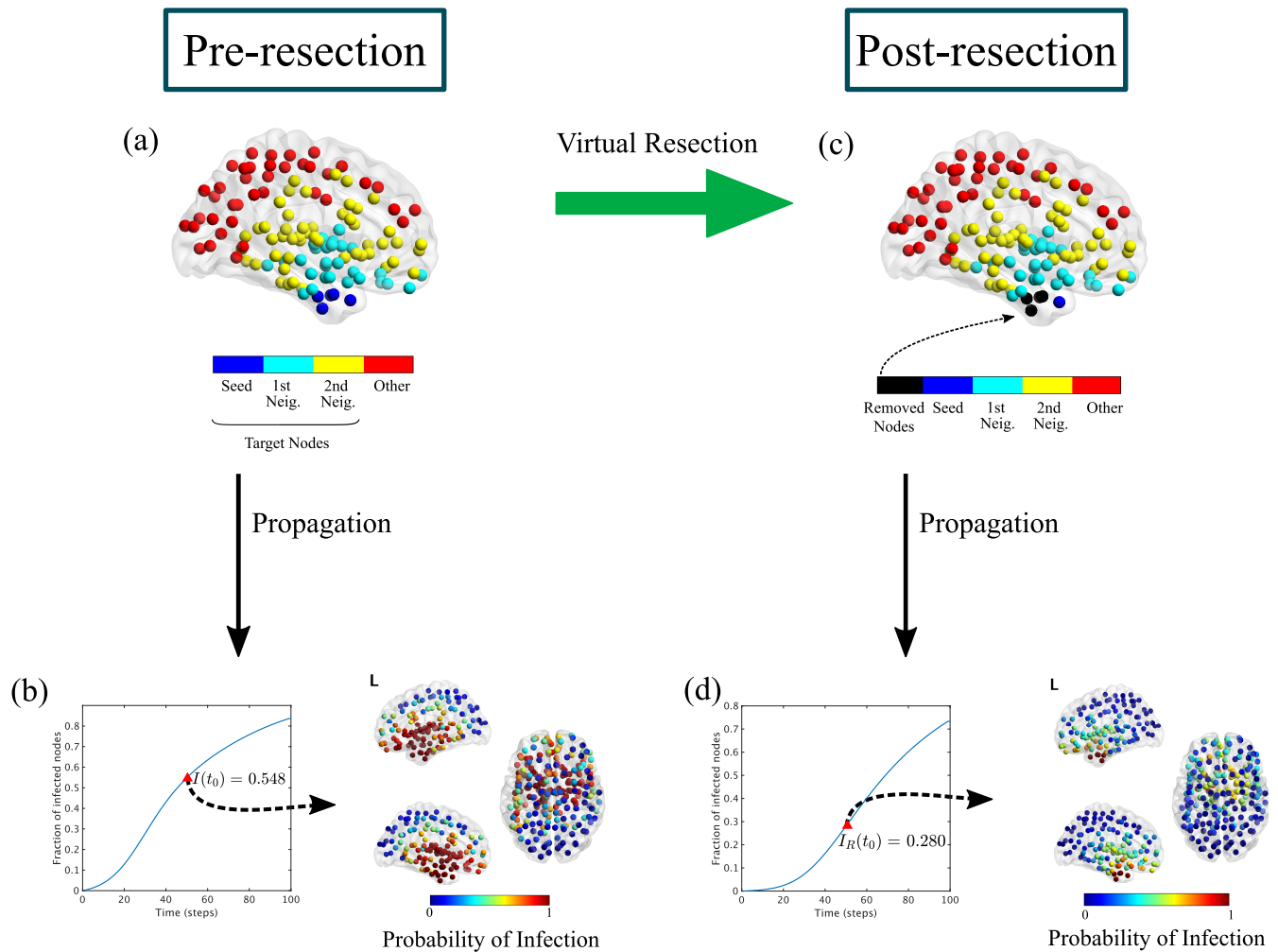
We defined a four-step method to find the optimal resection  $\mathcal{R}^*$  for each resection size  $S$ ,  $\mathcal{R}^*(S)$ . That is, the resection leading to a minimum propagation  $I_{\mathcal{R}^*(S)}(t_0)$ . The optimization method made use of the Simulated Annealing algorithm [77] to speed up the exploration of the space of possible resections, and it considered a surrogate structural metric – the mean *effective distance* to the seed [50, 57, 58] – as a proxy for the SI dynamics to simplify the initial exploration (the method and algorithms used are described in detail in the Supplementary Information and figure S1). Then, the smallest resection leading to a 90% reduction in seizure propagation (as measured by  $I_{\mathcal{R}}(t_0)$ ),  $\mathcal{R}_{90}$ , was identified. We also identified, for each patient, the smallest resection leading to 100% reduction in propagation ( $I_{\mathcal{R}}(t_0) = 0$ ),  $\mathcal{R}_{100}$ . Finally, to characterize the effect of small resections in seizure propagation, we also defined the one-node resection,  $\mathcal{R}_1$ , as the resection of size 1 with a maximum effect.

In principle all nodes in the network could be considered as possible targets to be resected. However, the effect of each node on seizure propagation decreases as it gets further from the seed (in terms of hops on the network). Therefore, here we considered only nodes that were at most two hops (without taking into account the edge weights) away from the seed (that is, the seed and its first and second neighbours), as depicted in figure 5a.

## 2.6 Statistics

The Mann-Whitney U test was used to determine the correlation between the modelled and clinical seizure propagation patterns. To compare the optimal correlation obtained with different network definitions we used a paired Student's t-test. Similarly, different seed definitions were compared using a paired Student's t-test. Finally, for comparisons between SF and NSF patients, we used an unpaired Student's t-test. All significance thresholds were set at  $p < 0.05$ .

Finally, analyzed the effect of the size and mean degree of the resection area on the size of the 90% and 100% resections, and on the effect of the one-node resection, with a linear least squares fit.



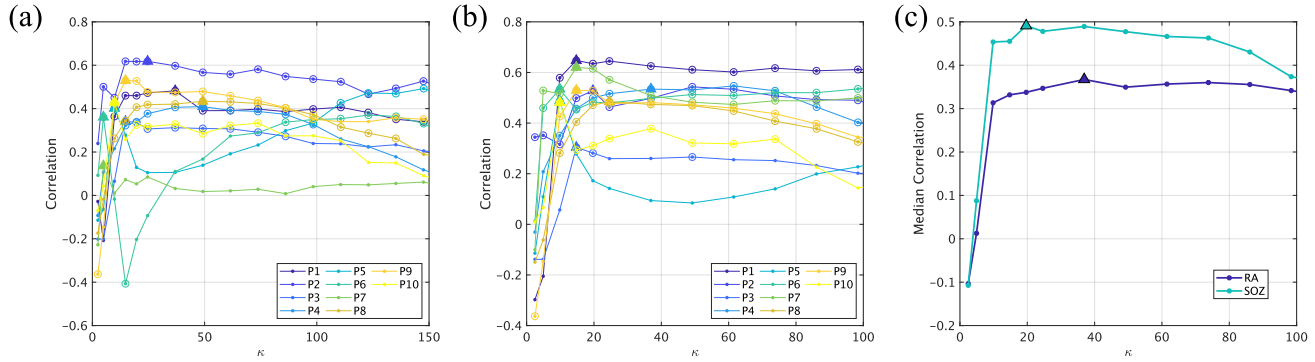


Figure 6: **Reproduction of seizure propagation.** Correlation between the modelled and clinically observed seizure propagation patterns as a function of network density, for each patient, using the RA (panel **a**) and SOZ seeds (panel **b**). Panel (**c**) indicates the median curves for each case, as indicated by the legend. Circles in panels **a** and **b** denote significant correlations ( $p < 0.05$ ), and the optimal correlation for each case is marked with a triangle.

## 2.7 Data availability

The data used for this manuscript are not publicly available because the patients did not consent for the sharing of their clinically obtained data. Requests to access to the datasets should be directed to the corresponding author. All user-developed codes are available from the corresponding author upon reasonable request.

## 3 Results

### 3.1 Preliminary results

A total of 10 patients (5 females) were included in the study, 7 of whom were deemed SF one year after surgery (see table 1 for the patient details).

We obtained the individual weighted MEG functional connectivity networks, with entries  $w_{ij}$  characterizing the coupling strength between ROIs  $i$  and  $j$ , for each patient in the alpha-band and the broadband using the BNA atlas (246 nodes). The tables and figures shown in the main text report the results for the broadband networks, details for the alpha-band can be found in the Supplementary Information. An exemplary FC matrix is shown in figure 1.

We constructed a clinical propagation pattern from the seizures observed with SEEG, for each patient. The pattern was initially defined in term of the electrodes CP, and then translated into the ROIs of the BNA atlas (see figure 2).

### 3.2 Reproduction of Seizure Propagation Patterns

As described in the methods section (see figure 4), we estimated the correlation  $C$  between the SI seizure pattern and the SEEG pattern for a range of connectivity values  $\kappa$ , as shown in figure 6a for the broadband networks and in figure S3 for the alpha-band networks. Then, to fit the spreading model to the SEEG propagation data, we selected the connectivity value  $\kappa_{\max}$  that maximized  $C(\kappa)$ , for each patient. The maximum correlation  $C_{\max}$  obtained for each patient and the corresponding  $\kappa_{\max}$  are shown in figure 7a,b for the broadband networks and in figure S4 for the alpha-band networks, and the corresponding values are reported in tables S1 and S2, respectively. Most cases presented a bimodal dependence of the correlation on the network density, so that there was a maximum for low density and another maximum for large density. Here we restrict our analyses to the first maximum, which yields only the fundamental connections that are needed to reproduce seizure propagation.

We found that the model significantly reproduced the seizure propagation patterns for 9/10 patients. The average correlation was  $C^\alpha = 0.38$  for the alpha-band ( $\alpha$ ) networks and  $C^{\text{BB}} = 0.41$  for the broad-band (BB) networks. The difference between the two settings (0.03,  $\text{BB} > \alpha$ ) was not significant ( $t(9) = 1.81$ ,  $p = 0.06$ ). There were no significant differences in the optimal correlation between SF and NSF patients ( $C_{\text{SF}}^\alpha - C_{\text{NSF}}^\alpha = -0.05$ ,  $p = 0.3$ ,  $t(8) = -0.41$ ;  $C_{\text{SF}}^{\text{BB}} - C_{\text{NSF}}^{\text{BB}} = -0.01$ ,  $p = 0.5$ ,  $t(8) = -0.07$ , unpaired Student t-tests).

336 The optimal network density did not differ significantly between frequency bands ( $\kappa^{\text{BB}} - \kappa^{\alpha} = 0.99$ ,  $p = 0.4$ ,  
337  $t(9) = 0.15$ ) or between the sub-groups ( $\kappa_{\text{SF}}^{\alpha} - \kappa_{\text{NSF}}^{\alpha} = 13.47$ ,  $p = 0.05$ ,  $t(8) = 1.91$ ;  $\kappa_{\text{SF}}^{\text{BB}} - \kappa_{\text{NSF}}^{\text{BB}} = -16.75$ ,  
338  $p = 0.09$ ,  $t(8) = -1.50$ ).

### 3.2.1 Alternative Definition of the Seed

340 Different definitions of the seed can be considered. So far, we used the resection area, but in prospective studies  
341 the actual resection area will not be known. We therefore also considered the SOZ, as defined by the SEEG  
342 study, as the seed for the SI spreading (seed SOZ), and repeated the fit method as before (see figure 6b). We  
343 found that now the correlation between the model and the seizure pattern was significant for all patients, both  
344 for the alpha- and broad-band networks. The average correlations were respectively  $C^{\alpha} = 0.47$  and  $C^{\text{BB}} = 0.51$ .  
345 The difference ( $C^{\alpha} - C^{\text{BB}} = -0.04$ ) was significant ( $p = 0.04$ ,  $t(9) = -1.99$ ).

346 We found that the optimal correlation was higher for SF than for NSF patients ( $C_{\text{SF}}^{\alpha} - C_{\text{NSF}}^{\alpha} = 0.06$ ,  
347  $C_{\text{SF}}^{\text{BB}} - C_{\text{NSF}}^{\text{BB}} = 0.05$ ), although the difference was not significant (for  $\alpha$ -networks:  $p = 0.2$ ,  $t(8) = 0.79$ ; for BB  
348 networks:  $p = 0.2$ ,  $t(8) = 0.79$ ). The optimal network density did not differ significantly between frequency  
349 bands ( $\kappa^{\text{BB}} - \kappa^{\alpha} = -6.64$ ,  $p = 0.08$ ,  $t(9) = -1.52$ ) or between the sub-groups ( $\kappa_{\text{SF}}^{\alpha} - \kappa_{\text{NSF}}^{\alpha} = 6.80$ ,  $p = 0.2$ ,  
350  $t(8) = 0.79$ ;  $\kappa_{\text{SF}}^{\text{BB}} - \kappa_{\text{NSF}}^{\text{BB}} = -1.51$ ,  $p = 0.4$ ,  $t(8) = -0.25$ ).

351 Overall, this seed definition reproduced the clinical seizure pattern better than the RA seed ( $C^{\alpha}(\text{SOZ}) -$   
352  $C^{\alpha}(\text{RA}) = 0.09$ ,  $p = 0.07$ ,  $t(9) = 1.63$ ;  $C^{\text{BB}}(\text{SOZ}) - C^{\text{BB}}(\text{RA}) = 0.10$ ,  $p = 0.04$ ,  $t(9) = 1.99$ ), although the  
353 difference was only significant for broad-band networks.

### 3.2.2 Effect of Individualized Brain Networks

354 Is patient specific connectivity required to reproduce the clinically observed seizure propagation patterns? In  
355 order to answer this question, we repeated the analysis using the average functional connectivity matrix (referred  
356 to as AV- $\alpha$  and AV-BB respectively for the alpha-band and broadband networks) as the network backbone for  
357 the SI spreading dynamics for all patients.  
358

359 For the broad-band network, a significant correlation was found for 8 (10) patients using the RA (SOZ)  
360 seed (see figures 7 and S4). The average optimal correlation ( $C^{\text{AV-BB}}(\text{RA}) = 0.36$ ,  $C^{\text{AV-BB}}(\text{SOZ}) = 0.48$ ) was  
361 smaller than for the individual patient networks ( $C^{\text{BB}}(\text{RA}) - C^{\text{AV-BB}}(\text{RA}) = 0.05$ ,  $p = 0.08$ ,  $t(9) = 1.95$ ;  
362  $C^{\text{BB}}(\text{SOZ}) - C^{\text{AV-BB}}(\text{SOZ}) = 0.03$ ,  $p = 0.09$ ,  $t(9) = 1.92$ ), although the difference was not significant. For  
363 the alpha-band network, a significant correlation was found for 7 (10) patients using the RA (SOZ) seed. The  
364 average (optimal) correlation ( $C^{\text{AV-}\alpha}(\text{RA}) = 0.34$ ,  $C^{\text{AV-}\alpha}(\text{SOZ}) = 0.46$ ) was smaller than for the individual  
365 patient networks ( $C^{\alpha}(\text{RA}) - C^{\text{AV-}\alpha}(\text{RA}) = 0.05$ ,  $p = 0.2$ ,  $t(9) = 1.30$ ;  $C^{\alpha}(\text{SOZ}) - C^{\text{AV-}\alpha}(\text{SOZ}) = 0.01$ ,  $p = 0.8$ ,  
366  $t(9) = 0.28$ ) but the difference was not significant.

### 3.2.3 Average model

367 Above, the optimal network connectivity was fitted independently for each patient using the SEEG data. In  
368 order to test if a mean model could be used for patients without SEEG recordings, we have estimated the median  
369 correlation yielded by the model for each connectivity value, as depicted in figure 6c for BB-networks and figure  
370 S3c for  $\alpha$ -band networks, both for the RA and SOZ seeds. For BB-networks, the maximum overall correlations  
371 found were  $C_m^{\text{BB}}(\text{RA}) = 0.37$  for  $\kappa = 36.90$  for the RA seed; and  $C_m^{\text{BB}}(\text{SOZ}) = 0.49$  for  $\kappa = 19.68$  for the SOZ  
372 seed. For  $\alpha$ -band networks, the maximum overall correlations found are  $C_m^{\alpha}(\text{RA}) = 0.33$  for  $\kappa = 19.68$  for the  
373 RA seed; and  $C_m^{\alpha}(\text{SOZ}) = 0.45$  for  $\kappa = 19.68$  for the SOZ seed. These values were smaller than the mean optimal  
374 results ( $C^{\text{BB}}(\text{RA}) = 0.41$ ,  $C^{\text{BB}}(\text{SOZ}) = 0.51$ ,  $C^{\alpha}(\text{RA}) = 0.38$ ,  $C^{\alpha}(\text{SOZ}) = 0.47$ ), but the decrease was less than  
375 15% on average and not significant ( $t(9) = 1.95$ ,  $p = 0.08$  and  $t(9) = 1.90$ , respectively for the  $\alpha$ -band and BB  
376 networks).  
377

### 3.2.4 Comparison with Fully Connected Networks

378 We also compared the correlation results with those obtained using a trivial fully connected network. Correlation  
379 results for this structure are shown in figures 7 and S4, together with the results obtained with individual broad-  
380 band networks (averaged) and when using the average broad-band network. Although the fully connected  
381 network achieved a significant correlation for some patients (3 patients for the RA seed and 5 for the SOZ seed),  
382 the correlation was always lower than for the individually optimised model, except for one patient using the SOZ  
383 seed, and the average was significantly smaller ( $C^{\text{BB}}(\text{RA}) - C^{\text{FCN}}(\text{RA}) = 0.29$ ,  $p = 1.4 \cdot 10^{-4}$ ,  $t(9) = -6.27$ ;  
384  $C^{\text{BB}}(\text{SOZ}) - C^{\text{FCN}}(\text{SOZ}) = 0.22$   $p = 0.005$ ,  $t(9) = 3.72$ ;  $C^{\alpha}(\text{RA}) - C^{\text{FCN}}(\text{RA}) = 0.27$ ,  $p = 7 \cdot 10^{-4}$ ,  $t(9) = 5.01$ ;  
385  $C^{\alpha}(\text{RA}) - C^{\text{FCN}}(\text{SOZ}) = 0.18$ ,  $p = 0.013$ ,  $t(9) = 3.09$ ).

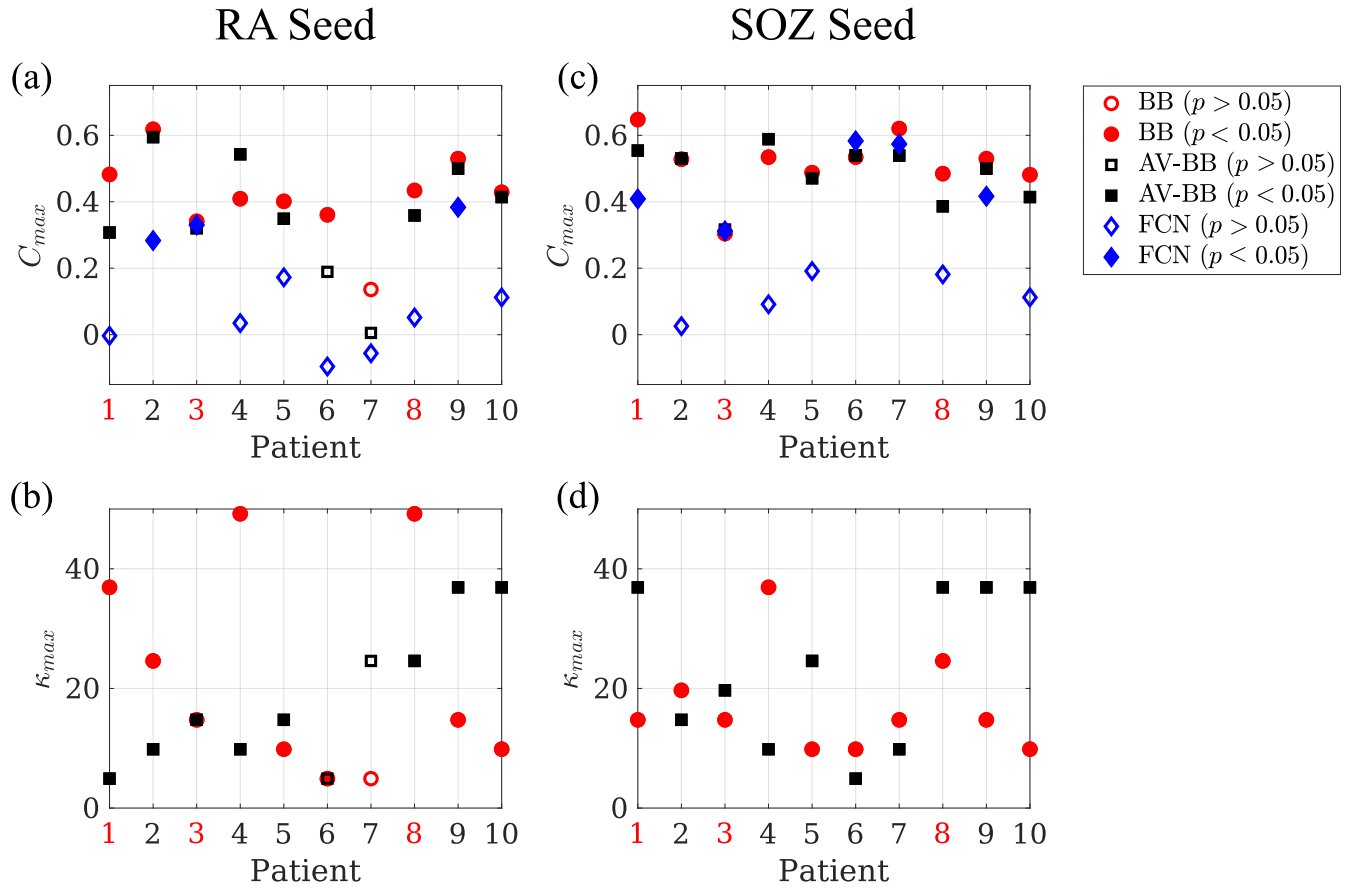


Figure 7: **Reproduction of seizure propagation patterns.** Panels (a) and (c) show the average maximum correlation  $C_{max}$  achieved by the individual BB networks (BB, red circles), and the average BB one (AV-BB, black squares), and the correlation found for the fully connected network (FCN, blue diamonds), respectively for the RA and SOZ seeds. Panels (b) and (d) show the corresponding  $\kappa_{max}$  for the individual (BB, red circles) and average (AV-BB, black squares) networks. Significant correlations ( $p < 0.05$ ) are indicated by a filled marker, and non-significant ones ( $p > 0.05$ ) by an empty marker. NSF patients are indicated by red labels.

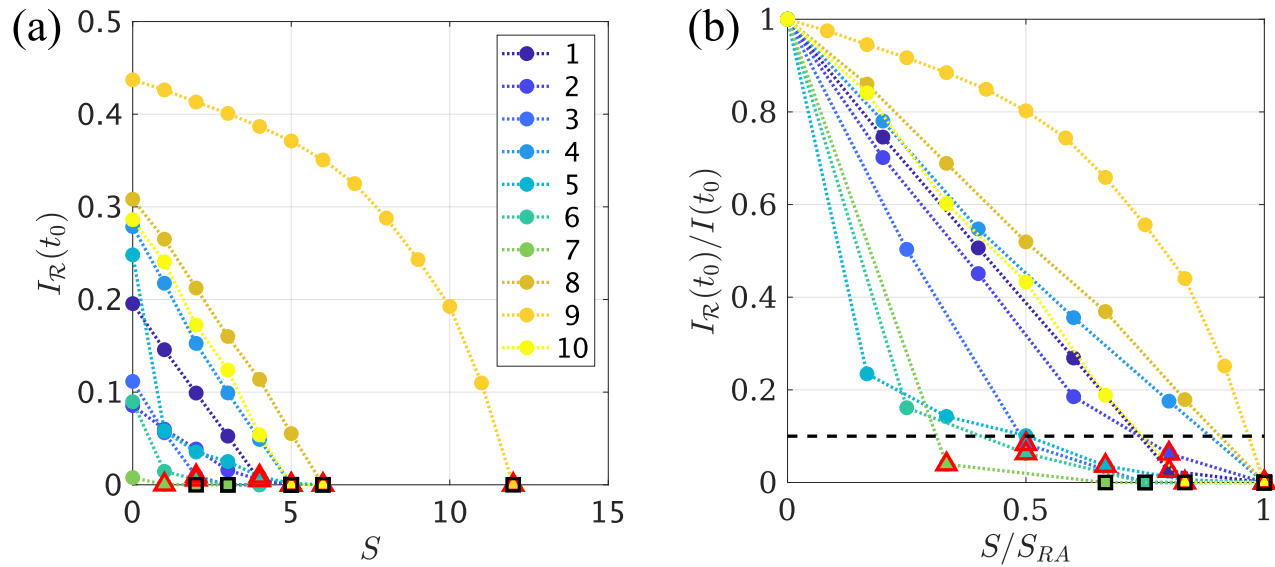


Figure 8: **Optimal Virtual Resection.** (a) Reduction in epidemic spreading for virtual resections of increasing size  $S$ , as quantified by the decrease in  $I_{\mathcal{R}}(t_0)$ . Each curve corresponds to one patient, as indicated in the legend. Red triangles mark the resection that achieved a 90% decrease in propagation,  $\mathcal{R}_{90}$ , and black squares the smallest resection that stopped seizure propagation,  $\mathcal{R}_{100}$ . (b) In order to enable comparison of the VRs performance between patients, we depict the normalized decrease in propagation,  $I_{\mathcal{R}}(t_0)/I(t_0)$  as a function of the normalized resection size,  $S/S_{RA}$ . The black dashed line indicates a 90% decrease in propagation.

### 3.3 Virtual Resection Analysis

387

388

389

390

391

392

393

394

395

396

397

398

399

400

401

402

403

404

405

406

407

408

409

410

411

412

413

414

415

We made use of the VR optimization method illustrated in figures 5 and S1 to find optimal virtual resections of increasing size  $S$ , for each patient. Results of the virtual resection analysis are shown in figure 8 for all patients. Propagation after the resection (as measured by  $I_{\mathcal{R}}(t_0)$ ) decreased as  $S$  increased for all patients. However, the exact trend that was followed depended on the individual network structure and seed size. Patients 3, 5 – 7 showed a rapid decrease of  $I_{\mathcal{R}}(t_0)(S)$  for small  $S$ , whereas patient 9 showed a slower (parabolic) decrease. The remaining patients showed approximately linear decreases.

Complete stop of seizure propagation was found for the trivial resection of size  $S = S_{RA}$ , which corresponds to complete removal of the seed, for all patients. However, in some cases the 100% resection  $\mathcal{R}_{100}$  (i.e. the smallest resection leading to a 100% decrease in seizure propagation) was smaller than resection area. This resection is indicated by black squares in figure 8. We found that  $\mathcal{R}_{100}$  was smaller than the resection area for 4 patients (patients 4, 6, 7 and 10). Moreover, for 7/10 patients we were able to find a resection  $\mathcal{R}_{90}$ , of smaller size than the actual resection, yet that achieved over 90% decrease in propagation, as indicated by red triangles in figure 8. The sizes of the  $\mathcal{R}_{90}$  and  $\mathcal{R}_{100}$  resections relative to the size of the resection area, i.e.  $s_{90} = S_{\mathcal{R}_{90}}/S_{RA}$  and  $s_{100} = S_{\mathcal{R}_{100}}/S_{RA}$ , are shown in figure 9a for all patients. On average,  $s_{90}$  was 74% (range: 33 – 100%), whereas the  $s_{100}$  was 90% (range: 67 – 100%).

The  $I_{\mathcal{R}}(S)$  curves shown in figure 8 indicate that, for some patients, performing just a one-node resection,  $\mathcal{R}_1$ , already had a large effect on (reducing) seizure propagation. This is explicitly shown by  $i_{\mathcal{R}_1} = I_{\mathcal{R}_1}(t_0)/I(t_0)$  in figure 9b. The average effect of the 1-node resection was a 58% reduction in seizure propagation, although this number varied greatly among patients (range: 4–97%).

We analyzed the effect of the seed size and its connectivity on these results (see Supplementary Information, figure S5) by correlating  $s_{90}$ ,  $s_{100}$  and  $i_{\mathcal{R}_1}$  respectively with the number of links with nodes that were in the resection area,  $E_{RA} = S_{RA} * \kappa_{RA}$ . We found that  $s_{90}$  and  $s_{100}$  correlated positively with  $E_{RA}$  ( $r(8) = 0.81$ ,  $p = 0.005$  and  $r(8) = 0.61$ ,  $p = 0.07$ , for  $s_{90}$  and  $s_{100}$ , respectively), although the correlation was only significant for  $s_{90}$ . On the contrary,  $i_{\mathcal{R}_1}$  correlated negatively with  $E_{RA}$  ( $r(8) = -0.71$ ,  $p = 0.02$ ). These results indicate that larger seed regions required a comparatively larger resection.

Finally, we analysed the location of the optimal resections found by the model (data not shown). We found that, for 1 patient, the optimal resection  $\mathcal{R}_{90}$  included nodes outside of the resection area and, similarly,  $\mathcal{R}_{100}$  was also found to include nodes outside of the resection area for another patient.



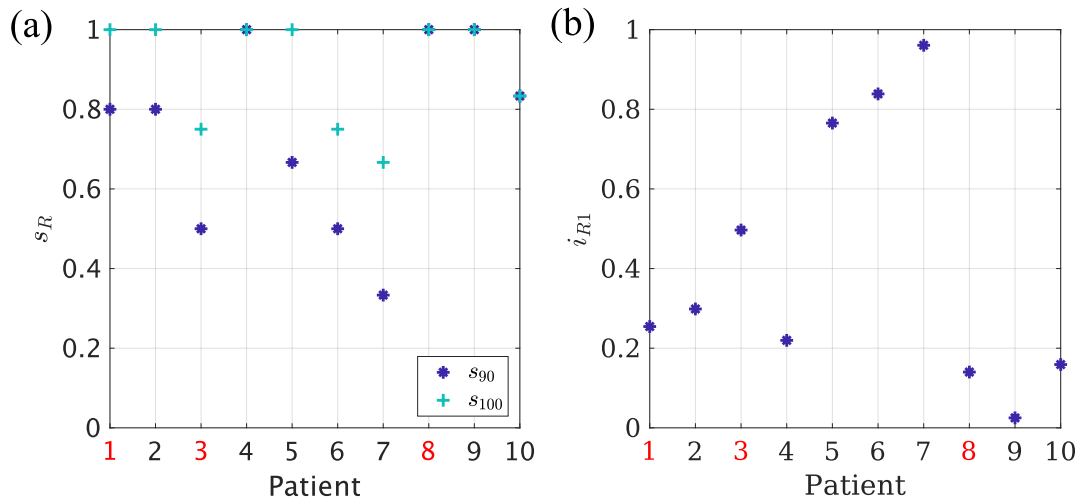


Figure 9: **Analysis of optimal virtual resections.** (a) Normalized size of the 90% ( $s_{90}$ , dark blue asterisks) and 100% ( $s_{100}$ , turquoise crosses) resections for each patient. (b) Normalized effect  $i_{R1} = I_{R1}(t_0)/I(t_0)$  of the one node resection, for each patient. NSF patients are indicated by red labels in both panels.

## 4 Discussion

We have defined a patient-specific seizure-propagation model based on the SI spreading dynamics. The model considers the patient-specific MEG functional connectivity matrix and makes use of clinical SEEG data to define stereotypical seizure propagation patterns for each patient. Seizure propagation was then modeled as an SI process propagating from a seed – which we initially took to be the patient’s resection area (RA) – to the rest of the network. Comparing the propagation patterns in the model to those observed clinically, we showed that this simple model reproduces the main aspects of the individual seizure propagation patterns, and that an alternative definition of the seed – based on the SEEG recordings – might provide a better reproduction of the observed propagation patterns. The main free parameter of the model – the network mean connectivity – was fitted to maximally reproduce the clinical seizure pattern, independently for each patient.

Using the model settings that optimally reproduced the clinically observed patterns, we then made use of the virtual resection technique to study alternative resections of smaller size or at different locations relative to the clinical resection area. The model suggested smaller virtual resections that were usually confined to the resection area, but in some cases included regions outside of the resected area.

### 4.1 Modeling Considerations

In this study we considered how individualized computer models, integrating patient-specific data from different modalities, can aid epilepsy surgery [26, 32–40, 42, 43, 78]. As opposed to previous studies which considered highly detailed, non-linear, stochastic models to simulate the activity of each brain region in detail [35, 37, 40, 43, 79–81], here we considered an abstract model of epidemic spreading, the SI model, as a proxy for seizure propagation dynamics (see figures 3 and 4). Epidemic models capture the basic mechanisms of processes that diffuse on networked systems, and have been used, for example, to study the propagation of pathological proteins on brain networks [52] and of ictal activity [41].

Moreover, epidemic models are supported by a well-grounded mathematical framework that can aid the exploration of the model. For instance, the fundamental role of hubs in seizure propagation is expected from a spreading perspective: hubs can act as super spreaders, being responsible for a disproportionate number of infections [54, 82], and their existence enhances epidemic spreading, both increasing the speed of propagation and decreasing the epidemic threshold [51]. On the contrary, a strong community structure can help control the epidemic, which may remain trapped in one community [83, 84]. This result also aligns with the clinical observation that often seizure propagation can be restricted to one or a few brain lobes [1], in the case of focal epilepsy. This is characterized by focal seizures that remain within some regions and only sometimes brake through the inhibitory “wall” and generalize. Interestingly, seizures originating in certain regions (such as the temporal lobes) are more likely to remain focal than others (such as frontal seizures). Similarly, other network

448 characteristics such as temporal changes in connectivity [85, 86] or degree correlations can also alter behavior of  
449 spreading processes [87].

450 Epidemic models can thus help us studying seizure propagation processes. Of the large family of such models,  
451 we have selected the SI model as it captures the basic nature of epidemic spreading processes, including seizure  
452 propagation [51]. It only considers one mechanism: the propagation of an infectious process (or a seizure)  
453 from one region to another. Consequently, there is only one free parameter in the model – the probability  
454 that the infection is transmitted. This comes at the cost of not allowing for region deactivation: the model  
455 can only describe the initial steps of seizure propagation, when the activity starts to spread out. More detailed  
456 propagation models – such as the Susceptible-Infected-Susceptible (SIS) or Susceptible-Infected-Recovered (SIR)  
457 models – do include deactivation mechanisms, but in doing so extra parameters are introduced that would need  
458 to be fine tuned or assumed upon. Moreover, the early propagation-dominated phase of the SIR model is highly  
459 similar to the SI model, and this is the regime of interest here.

460 As the backbone for seizure propagation in the model, we used the broad-band AEC-MEG functional con-  
461 nectivity network as a proxy for the structural brain network (see figure 1). By not correcting for the effect of  
462 volume conduction/field spread, short-range connections are present in the network [70–73], yet it also captures  
463 long-range connections that might be difficult to capture with DTI-based tractography. Moreover, the functional  
464 network is a good indicator of how activity spreads on the network and, as we have shown, it suffices to reproduce  
465 the SEEG seizure propagation patterns when used in combination with the SI model.

## 466 4.2 Reproduction of seizure propagation patterns

467 In many patients, seizures follow stereotypical activation patterns. In this study we selected 10 patients who  
468 showed clear patterns on the SEEG recordings (see figure 2), and compared seizure propagation in the model  
469 with those clinically observed patterns, as depicted in figure 4. Despite its simplicity, we found that the model  
470 reproduces the main characteristics of the individual seizure propagation patterns in 9/10 patients when the  
471 resection area was considered as the seed (see figures 6a and 7a,b). Moreover, by using the possible seizure onset  
472 zone, as indicated by the SEEG recordings, as the seed for epidemic spreading, we showed that the model is  
473 sensitive to different definitions of the seed, and that alternative definitions can improve on the reproduction of  
474 the clinical patterns (see figures 6b and 7c,d). We also found that patient specific connectivity reproduces seizure  
475 propagation better than fully connected networks, and marginally (although not significantly) better than the  
476 average connectivity network (see figure 7). This result is in line with previous studies [36, 41] in which possible  
477 benefits of using patient-specific connectivity were suggested, but could not be corroborated by a significant  
478 difference in the model. Likely, larger data sets would be necessary to unravel how the models benefit from  
479 considering patient-specific connectivity.

480 The density of connections of the network was set for each patient to fit the SEEG seizure propagation  
481 pattern. Higher density levels imply a more extended or homogeneous propagation pattern, whereas smaller ones  
482 are associated with a more well-defined propagation. Then, the SI propagation rate  $\beta$  was adjusted accordingly  
483 for each patient for the subsequent virtual resection analysis.

484 The model parameters were fitted to the patient’s SEEG data, hence the current definition of the model  
485 relies on the use of SEEG recordings to infer the patient-specific seizure-propagation patterns and fit the model  
486 free parameters. However, these are not always part of standard clinical practice, as they are highly invasive for  
487 the patient and not always needed during pre-surgical planning. In order to show the feasibility of applying the  
488 model to patients without such recordings, we have shown in figure 6c that the average optimal model parameters  
489 can be used as an approximate solution. The propagation of seizures typically makes use of existing pathways,  
490 many of which are not patient-specific and can be recovered by the average model parameters. In the current  
491 setting, considering the overall best threshold for the connectivity matrix, instead of the individual one, led to  
492 less than a 15% decrease in correlation between the modeled and clinical seizure-propagation patterns. Within  
493 this configuration, the model is still personalized, as it is still fitted specifically for each patient via the patient’s  
494 MEG based connectivity matrix and seed for the SI propagation dynamics. Moreover, if a larger data-base is  
495 constructed, the patients could be grouped by epilepsy type and different optimal type-specific thresholds could  
496 be defined.

497 For seizure-free (SF) patients the resection area is, by definition, a better representation of the epileptogenic  
498 zone than for non-seizure-free ones (NSF). Thus, one might expect that modelled epidemics spreading from the  
499 resection area might also reproduce the clinically observed seizure propagation patterns better for SF patients  
500 than for NSF ones. In order to test this hypothesis, we compared the correlations between the modelled and the  
501 clinical propagation patterns for SF and NSF patients. We found no significant differences for any of the cases  
502 considered (i.e. using either the resection area or the SEEG-based SOZ as seed). The limited spatio-temporal  
503 resolution of the clinical propagation profile might be partially accountable for this result. The small group size

504 (10 patients, only 3 of whom were NSF) prevents any further interpretations of this result. It is still worth  
505 noting, however, that in the current setting all patients had a big improvement in the frequency and severity  
506 of the seizures [2, 59], so the resection area provided a reasonable approximation for the EZ, even for the NSF  
507 patients.

### 508 4.3 Modelling Resections

509 The effect of different resections on seizure propagation can be studied with the model by implementing virtual  
510 resections (see figure 5). One can then search for optimal resections that minimize seizure propagation for a  
511 given resection size. This can be used to aid epilepsy surgery by either finding resections that are smaller than  
512 the standard clinical approach, but have the same or almost the same effect [41], to find alternative resections  
513 that avoid specific regions [40], such as eloquent cortex, or to propose alternative resections, including regions  
514 outside the hypothesized SOZ, that might lead to a better outcome for NSF patients.

515 The problem of optimization of virtual resections is highly computationally demanding. We found that a  
516 method that combines topological – using a surrogate structural measure [57, 58] – and dynamical properties  
517 can find optimal resections on the network. The use of this surrogate measure allows for a fast exploration of the  
518 space of possible resections, which is followed by a slower analysis using the SI dynamics to fine-tune the solution  
519 and measure the actual decrease in seizure propagation. In future studies exact results of the SI propagation on  
520 a network could also be implemented to avoid the need for random search methods [75, 88], taking advantage of  
521 the mathematical tractability of the SI model.

522 The effect of a resection in the model was measured as the decrease in propagation at a given time  $t_0$ . That  
523 is, we measured the slowing down of seizure propagation due to the resection. In the model, a complete stop  
524 of propagation can only be achieved with – and is always achieved by – the complete disconnection of the seed  
525 from the rest of the network (this may not imply complete seed removal, in some cases removal of the nodes  
526 connecting the seed to the rest of the network might be enough and more efficient). This is because in the SI  
527 model activity always spreads to every connected region, eventually, regardless of any other network or model  
528 parameter. However, this model is only an approximation of actual seizure propagation, which is assumed to  
529 hold only for small times in which seizure dynamics are dominated by the activity propagation processes. After  
530 that, deactivation mechanisms kick in and the epileptiform activity eventually dies out. Within this paradigm,  
531 a sufficient decrease in seizure propagation at a given (early) time  $t_0$  would be enough to indicate an effective  
532 resection (that is likely to lead to seizure freedom); here this threshold was set to 90% of the original infection  
533 rate at time  $t_0$ . Thus, we defined the optimal resection for each patient as the smallest resection leading to at  
534 least 90% decrease in seizure propagation. We found in the model that this optimal resection was smaller than  
535 the actual resection area for 7 out of 10 patients. Moreover, for four patients we found that it was possible to stop  
536 seizure propagation at the fixed time  $t_0$  with a resection smaller than the resection area. We found that cases  
537 with a larger or more densely connected epileptogenic region (i.e. a larger seed for the SI dynamics) required a  
538 larger portion of the seed to be removed to consistently reduce seizure propagation.

539 These findings highlight the need to devise patient-specific models to aid epilepsy surgery planning, so that  
540 optimized individualized resections with minimal side-effects can be found. In this study we allowed the search  
541 algorithm to consider nodes outside the resection area as targets for the virtual resections. We found that, for  
542 one patient, the optimal 90% resection included one node outside the RA, and similarly for another patient the  
543 100% resection also included one node outside the resection area. Thus, individualized models could in some  
544 cases suggest alternative resections outside of the suspected epileptogenic zone that might be more beneficial  
545 than standard surgery.

546 The 90% threshold for the reduction in seizure propagation was set ad-hoc and was equal for all patients, which  
547 might not be realistic. Future studies could include a patient-specific estimation of the propagation threshold by  
548 analyzing the individual intracranial EEG recordings: often epileptiform activity appears in a confined region  
549 but does not propagate to the rest of the network. Information about the size of this region could be used to  
550 estimate the threshold for which a reduction in seizure propagation in the model is considered sufficient, that  
551 is, for which the modelled activity remains within this local region. Alternatively, de-activation mechanisms  
552 could be introduced in the dynamical model, such as in the SIR model [41]. By setting the model initially in  
553 the super-critical regime – in which seizures have a non-zero probability of propagating, the optimal resection  
554 would be the one that takes the model to the subcritical regime with the minimum resection size. However, the  
555 parameters of the model – namely the propagation and de-activation probabilities – would strongly affect this  
556 result: if the system is initially far into the super-critical regime, a larger resection will be necessary compared to  
557 when it is close to the critical transition. In fact, the SI model as it was used here corresponds to the highly-super  
558 critical case in which seizures always spread. Thus, in order to avoid more assumptions that would hinder the  
559 interpretation of the outcomes of such a model, the SIR parameters would need to be tuned with clinical data,

560 using for instance high-resolution spatio-temporal seizure-propagation patterns [36, 44, 89].

### 561 **4.3.1 Alternative Resections for NSF patients**

562 Another implication of the model definition is the fact that complete removal or isolation of the seed always leads  
563 to complete stop of seizure propagation, because seizures, in the model, only generate within the seed. Within  
564 the current formulation of the model, the seed is defined ad-hoc from the clinical data, either according to the  
565 resection area (RA seed) or the pre-surgical clinical information (SOZ seed). This implies that the resection  
566 model cannot distinguish situations where the selected seed is not a good representation of the EZ, such as is  
567 the case for NSF patients, and suggest a better resection. The first part of the model, i.e. the reproduction of  
568 seizure propagation patterns, could be of aid: the plausibility of different seeds can be judged from the maximum  
569 correlation that they yield between the modelled seizure patterns and the clinical SEEG patterns. Thus, optimal  
570 seed definitions that maximally reproduce the observed seizure propagation patterns could be suggested. This  
571 hypothesis implies that a higher correlation should be found for SF than for NSF patients when considering  
572 the resection area as the seed, which we were not able to validate in this study due to the small group size.  
573 Future studies should tackle this issue with larger patient groups and possibly more detailed spatio-temporal  
574 seizure propagation patterns, to increase the model resolution. Moreover, this would also validate whether the  
575 model can provide independent information prospectively – that is, prior to surgery – and suggest optimal seed  
576 definitions.

## 577 **4.4 Strengths**

578 The main strength of our approach is the simplicity of the model considered. Epidemic spreading models do  
579 not intent to capture the details of the underlying biological basis of seizure generation and propagation, only  
580 the stereotypical patterns of seizure propagation [78]. The simplicity of the model not only allows for faster  
581 calculations and fewer free parameters, but it also comes with a large body of theoretical and computational  
582 studies that can be used to interpret the results and design the study [51].

583 We integrated data from different modalities that are commonly measured in clinical practice: MEG and  
584 SEEG recordings, and the location of the resection area. The use of MEG networks as a proxy for structural  
585 networks avoids the computation of structural DTI networks, which are not part of standard clinical care and also  
586 time-consuming, limiting the flexibility with which the choice of atlas can be changed. Using MEG functional  
587 networks to define the backbone for the dynamical model allows for more versatility, as well as the ability to use  
588 our approach in patients for whom DTI data are not available.

589 The model was fitted with patient-specific data and optimized independently for each patient. The varying  
590 results for different patients, both for the reproduction of seizure propagation patterns and the analysis of  
591 alternative resections, highlight the need for using personalized models of seizure propagation [36, 41, 89].

592 Moreover, the model could be easily extended to include more clinical presurgical information, such as the  
593 existence of MRI or MEG abnormalities. Similarly, the model could be used prospectively by using alternative  
594 definitions of the seed, that do not depend on the resection area, as we have already shown here by using seeds  
595 based on the SOZ as determined from SEEG (see figures 6 and 7).

## 596 **4.5 Limitations**

597 The main limitations of the current study are the limited number of patients considered and the low-resolution of  
598 the clinical seizure propagation patterns. The small cohort prevents further validation of the model to distinguish  
599 between SF and NSF patients. Meanwhile, the low resolution implies that few parameters of the dynamical model  
600 can be fit to the data.

601 Another important limitation is that the seed of seizure propagation was assumed from the data – being  
602 either the resection area or the SOZ as estimated from the SEEG recordings. This, in conjunction with the fact  
603 that complete removal of the seed always leads to a stop of seizure propagation, implies that the model cannot  
604 suggest better resections for NSF patients, and it also limits its prospective use. To be of more clinical use, the  
605 model should be able to suggest the seed of seizure propagation. This could be done by finding the set of nodes  
606 that maximally reproduces the clinical seizure propagation patterns. However, in order to do this realistically  
607 and in a systematic manner, more detailed spatio-temporal patterns of seizure propagation are needed for each  
608 patient. These could be obtained from the SEEG recordings directly [36, 44, 89].

609 Another limitation is the nature of the SI model: it reproduces adequately the initial steps of seizure prop-  
610 agation, but the lack of a de-activation mechanism means that it cannot fit the whole seizure. Including a

611 mechanism for de-activation would circumvent this issue, provided that the extra parameters can be adequately  
612 fitted.

613 The use of SEEG data to fit the model can be another limitation for its clinical use, as SEEG recordings  
614 are highly invasive and not always part of the presurgical evaluation. However, we have shown that the model  
615 parameters can be extrapolated from the overall best fit (see figure 6c) and used for patients without SEEG.  
616 In the current setting, this led to a less than 15% decrease in the reproducibility of the seizure patterns, as  
617 measured by the correlation between the SI and SEEG propagation patterns. Information from other modalities  
618 could also potentially be included, such as epileptiform abnormalities found in MEG imaging. These can be used  
619 to set the probability for a region being a seed region.

620 An inherent limitation of all studies analyzing the functional effect of different resections is modeling the  
621 resection itself. Here we have employed the commonly used *virtual resection* technique, such that the weights  
622 of all resected links are set to 0 [37, 79, 90, 91]. This does not account for the generalized effect that a local  
623 resection can have on the network [92]. It does not consider any plasticity mechanisms either [93, 94], which are  
624 known to occur following a lesion in the brain [11, 95] – and in particular following a resection [96–99]. These  
625 appear as a consequence of the network disruption, and can have widespread effects. They will play a significant  
626 role in the cognitive functioning following the resection, and can also affect the long-term outcome of the surgery.  
627 These effects should be included in future studies for a more comprehensive modelling of epilepsy surgery.

628 A final limitation of the study, and of similar studies using the virtual resection technique, is the difficulty  
629 of the validation of the results, as the different resections cannot be tested clinically. Typically, virtual resection  
630 models are validated by comparing the overlap between the suspected EZ as generated by the model with the  
631 resection area for both SF and NSF patients, where a valid model should provide a good match for SF patients  
632 and a poor match for NSF patients [32, 35, 37, 38, 42]. Alternatively, the propagation pathways simulated by  
633 the model are compared with those recorded with SEEG [36, 89]. We have undertaken the later approach in this  
634 work to tune the model parameters and for validation, and the first approach was used for validation, although  
635 the small group sizes do not allow us to draw strong conclusions in this proof-of-principle study. Moreover, using  
636 surgical outcome to validate the model is only a first step, as the ultimate goal is to improve surgical outcome,  
637 i.e. to perform the analysis proposed in this work before surgery has taken place.

## 638 4.6 Outlook

639 In recent years there have been increasing efforts to develop individualized computer models to study brain  
640 disorders. In particular, in the case of epilepsy surgery, it is expected that such models might help improve  
641 surgery outcome and decrease the cognitive side-effects associated with epilepsy surgery, by proposing targeted,  
642 individualized resections for each patient. Currently, the greatest challenge remains in the validation of the  
643 models, as the ground truth is inherently missing and the actual effect of a resection can only be known several  
644 months – or years – after the surgery has taken place. Thus, extensive retrospective validation of the models is  
645 necessary before prospective (or even pseudo-prospective) studies can take place. Here, the seizure propagation  
646 model ought to be validated in future studies by increasing the number of included patients, and the resolution  
647 of the SEEG seizure propagation pattern should be increased in order to increase the sensitivity to the model  
648 parameters. Then, if a better relation between the model and the clinical data can be found for SF than for NSF  
649 patients, as we have hypothesized, the model could be used to find the seed regions that maximally reproduce  
650 the seizure patterns. Similarly, future studies could explicitly include forbidden areas that cannot be removed  
651 during the surgery, such as the eloquent cortex, or avoid surgeries that are not possible in clinical practice.

## 652 5 Conclusions

653 Patient-specific epidemic models can capture the fundamental aspects of seizure propagation as observed clini-  
654 cally with invasive SEEG recordings. The models, optimized specifically for each patient, can then be used to test  
655 the effect that different resection strategies may have on seizure propagation *in silico*. Our results highlight the  
656 need for individualized computer models to aid epilepsy surgery planning by defining smaller targeted resections  
657 with potentially fewer side-effects and better outcome than standard surgery.

## 658 6 Acknowledgements

659 Ana P. Millán and Ida A. Nissen were supported by ZonMw and the Dutch Epilepsy Foundation, project number  
660 95105006. The funding sources had no role in study design, data collection and analysis, interpretation of results,  
661 decision to publish, or preparation of the manuscript.



## 7 Competing Interests

The authors declare that they have no competing interests.

## 8 Author Contributions

A.P.M., E.C.W.S., C.J.S., I.A.N, A.H. conceptualized the study, E.C.W.S., C.J.S., I.A.N, S.I., J.C.B., P.V.M., A.H. participated in the funding acquisition, A.P.M, E.C.W.S., C.J.S, A.H. devised the Methodology, A.P.M. performed the formal analysis, A.P.M, I.A.N, A.H. devised the software and visualization E.C.W.S., C.J.S., P.V.M., A.H. participated in the supervision, E.C.W.S., S.I., J.C.B. provided resources, A.P.M. wrote the original draft and all authors participated in writing review and editing.

## References

- [1] P. N. Banerjee, D. Filippi, and W. A. Hauser. “The descriptive epidemiology of epilepsy—a review”. *Epilepsy Research* 85.1 (2009).
- [2] A. T. Berg et al. “Revised terminology and concepts for organization of seizures and epilepsies: report of the ILAE Commission on Classification and Terminology, 2005–2009”. *Epilepsia* 51.4 (2010).
- [3] O. C. González et al. “Ionic and synaptic mechanisms of seizure generation and epileptogenesis”. *Neurobiology of Disease* 130 (2019).
- [4] K. Lehnertz et al. “Synchronization phenomena in human epileptic brain networks”. *Journal of Neuroscience Methods* 183.1 (2009).
- [5] F. L. Da Silva et al. “Epilepsies as dynamical diseases of brain systems: basic models of the transition between normal and epileptic activity”. *Epilepsia* 44 (2003).
- [6] P. Kwan et al. “Definition of drug resistant epilepsy: consensus proposal by the ad hoc Task Force of the ILAE Commission on Therapeutic Strategies”. *Epilepsia* 51.6 (2010).
- [7] D. J. Englot et al. “Epileptogenic zone localization using magnetoencephalography predicts seizure freedom in epilepsy surgery”. *Epilepsia* 56.6 (2015).
- [8] B. C. Jobst and G. D. Cascino. “Resective epilepsy surgery for drug-resistant focal epilepsy: a review”. *Jama* 313.3 (2015).
- [9] H. O. Lüders et al. “The epileptogenic zone: general principles”. *Epileptic Disorders* 8.2 (2006).
- [10] M. A. Kramer and S. S. Cash. “Epilepsy as a disorder of cortical network organization”. *The Neuroscientist* 18.4 (2012).
- [11] C. J. Stam. “Modern network science of neurological disorders”. *Nature Reviews Neuroscience* 15.10 (2014).
- [12] E. H. Smith and C. A. Schevon. “Toward a mechanistic understanding of epileptic networks”. *Current neurology and neuroscience reports* 16.11 (2016).
- [13] L. Douw et al. “Epilepsy is related to theta band brain connectivity and network topology in brain tumor patients”. *BMC Neuroscience* 11.1 (2010).
- [14] M. Pedersen et al. “Increased segregation of brain networks in focal epilepsy: an fMRI graph theory finding”. *NeuroImage: Clinical* 8 (2015).
- [15] G. Bettus et al. “Decreased basal fMRI functional connectivity in epileptogenic networks and contralateral compensatory mechanisms”. *Human Brain Mapping* 30.5 (2009).
- [16] Z. Zhang et al. “Altered functional–structural coupling of large-scale brain networks in idiopathic generalized epilepsy”. *Brain* 134.10 (2011).
- [17] M. Centeno and D. W. Carmichael. “Network connectivity in epilepsy: resting state fMRI and EEG–fMRI contributions”. *Frontiers in Neurology* 5 (2014).



- 705 [18] G. J. Ortega et al. “Impaired mesial synchronization in temporal lobe epilepsy”. *Clinical Neuro-*  
706 *physiology* 122.6 (2011).
- 707 [19] G. Bettus et al. “Interictal functional connectivity of human epileptic networks assessed by intrac-  
708 *erebral EEG and BOLD signal fluctuations*”. *PLoS ONE* 6.5 (2011).
- 709 [20] F. Pittau et al. “Patterns of altered functional connectivity in mesial temporal lobe epilepsy”.  
710 *Epilepsia* 53.6 (2012).
- 711 [21] M. P. van den Heuvel and O. Sporns. “Network hubs in the human brain”. *Trends in cognitive*  
712 *sciences* 17.12 (2013).
- 713 [22] N. A. Crossley et al. “The hubs of the human connectome are generally implicated in the anatomy  
714 of brain disorders”. *Brain* 137.8 (2014).
- 715 [23] R. J. Morgan and I. Soltesz. “Nonrandom connectivity of the epileptic dentate gyrus predicts a  
716 major role for neuronal hubs in seizures”. *Proceedings of the National Academy of Sciences* 105.16  
717 (2008).
- 718 [24] B. C. Bernhardt et al. “Graph-theoretical analysis reveals disrupted small-world organization of  
719 cortical thickness correlation networks in temporal lobe epilepsy”. *Cerebral Cortex* 21.9 (2011).
- 720 [25] S.-H. Jin, W. Jeong, and C. K. Chung. “Mesial temporal lobe epilepsy with hippocampal sclerosis  
721 is a network disorder with altered cortical hubs”. *Epilepsia* 56.5 (2015).
- 722 [26] W. Liao et al. “Altered functional connectivity and small-world in mesial temporal lobe epilepsy”.  
723 *PLoS ONE* 5.1 (2010).
- 724 [27] I. A. Nissen et al. “Identifying the epileptogenic zone in interictal resting-state MEG source-space  
725 networks”. *Epilepsia* 58.1 (2017).
- 726 [28] S. Tavakol et al. “Neuroimaging and connectomics of drug-resistant epilepsy at multiple scales:  
727 From focal lesions to macroscale networks”. *Epilepsia* 60.4 (2019).
- 728 [29] I. Najm et al. “Temporal patterns and mechanisms of epilepsy surgery failure”. *Epilepsia* 54.5  
729 (2013).
- 730 [30] I. A. Nissen et al. “Localization of the epileptogenic zone using interictal MEG and machine  
731 learning in a large cohort of drug-resistant epilepsy patients”. *Frontiers in Neurology* 9 (2018).
- 732 [31] J. Hebbink et al. “Phenomenological network models: Lessons for epilepsy surgery”. *Epilepsia*  
733 58.10 (2017).
- 734 [32] M. A. Lopes et al. “An optimal strategy for epilepsy surgery: Disruption of the rich-club?” *PLoS*  
735 *Computational Biology* 13.8 (2017).
- 736 [33] F. Hutchings et al. “Predicting surgery targets in temporal lobe epilepsy through structural con-  
737 *nectome based simulations*”. *PLoS Computational Biology* 11.12 (2015).
- 738 [34] C. Yang et al. “Localization of epileptogenic zone with the correction of pathological networks”.  
739 *Frontiers in Neurology* 9 (2018).
- 740 [35] M. Goodfellow et al. “Estimation of brain network ictogenicity predicts outcome from epilepsy  
741 surgery”. *Scientific Reports* 6.1 (2016). Number: 1 Publisher: Nature Publishing Group.
- 742 [36] T. Proix et al. “Individual brain structure and modelling predict seizure propagation”. *Brain* 140.3  
743 (2017). Publisher: Oxford Academic.
- 744 [37] N. Sinha et al. “Predicting neurosurgical outcomes in focal epilepsy patients using computational  
745 modelling”. *Brain* 140.2 (2017). Publisher: Oxford Academic.
- 746 [38] A. Steimer, M. Müller, and K. Schindler. “Predictive modeling of EEG time series for evaluating  
747 surgery targets in epilepsy patients”. *Human Brain Mapping* 38.5 (2017).
- 748 [39] P. N. Taylor, M. Kaiser, and J. Dauwels. “Structural connectivity based whole brain modelling in  
749 epilepsy”. *Journal of Neuroscience Methods* 236 (2014).

- 750 [40] S. An et al. “Optimization of surgical intervention outside the epileptogenic zone in the Virtual  
751 Epileptic Patient (VEP)”. *PLoS Computational Biology* 15.6 (2019).
- 752 [41] I. A. Nissen et al. “Optimization of epilepsy surgery through virtual resections on individual  
753 structural brain networks”. *Research Square Preprint 10.21203/rs.3.rs-344720/v1* (2021).
- 754 [42] M. A. Lopes et al. “Elevated ictal brain network ictogenicity enables prediction of optimal seizure  
755 control”. *Frontiers in Neurology* 9 (2018).
- 756 [43] P. Laiou et al. “Quantification and selection of ictogenic zones in epilepsy surgery”. *Frontiers in  
757 Neurology* 10 (2019).
- 758 [44] V. Sip et al. “Data-driven method to infer the seizure propagation patterns in an epileptic brain  
759 from intracranial electroencephalography”. *PLoS Computational Biology* 17.2 (2021).
- 760 [45] M. A. Lopes et al. “Computational modelling in source space from scalp EEG to inform presurgical  
761 evaluation of epilepsy”. *Clinical Neurophysiology* 131.1 (2020).
- 762 [46] M. J. Koepp and F. G. Woermann. “Imaging structure and function in refractory focal epilepsy”.  
763 *The Lancet Neurology* 4.1 (2005).
- 764 [47] G. L. Barkley. “Controversies in neurophysiology. MEG is superior to EEG in localization of  
765 interictal epileptiform activity: Pro”. *Clinical Neurophysiology* 115.5 (2004).
- 766 [48] J. S. Ebersole and S. M. Ebersole. “Combining MEG and EEG source modeling in epilepsy eval-  
767 uations”. *Journal of Clinical Neurophysiology* 27.6 (2010).
- 768 [49] L. Junges et al. “The role that choice of model plays in predictions for epilepsy surgery”. *Scientific  
769 Reports* 9.1 (2019).
- 770 [50] A. Barrat, M. Barthelemy, and A. Vespignani. *Dynamical processes on complex networks*. Cam-  
771 bridge University Press, 2008.
- 772 [51] R. Pastor-Satorras et al. “Epidemic processes in complex networks”. *Reviews of Modern Physics*  
773 87.3 (2015).
- 774 [52] L. R. Peraza et al. “Structural connectivity centrality changes mark the path toward Alzheimer’s  
775 disease”. *Alzheimer’s & Dementia: Diagnosis, Assessment & Disease Monitoring* 11 (2019).
- 776 [53] C. J. Stam et al. “The relation between structural and functional connectivity patterns in complex  
777 brain networks”. *International Journal of Psychophysiology. Research on Brain Oscillations and  
778 Connectivity in A New Take-Off State* 103 (2016).
- 779 [54] J. O. Lloyd-Smith et al. “Superspreading and the effect of individual variation on disease emer-  
780 gence”. *Nature* 438.7066 (2005).
- 781 [55] R. Pastor-Satorras and A. Vespignani. “Immunization of complex networks”. *Physical review E*  
782 65.3 (2002).
- 783 [56] Z. Dezsó and A.-L. Barabási. “Halting viruses in scale-free networks”. *Physical Review E* 65.5  
784 (2002).
- 785 [57] D. Brockmann and D. Helbing. “The hidden geometry of complex, network-driven contagion phe-  
786 nomena”. *Science* 342.6164 (2013).
- 787 [58] P. C. Pinto, P. Thiran, and M. Vetterli. “Locating the source of diffusion in large-scale networks”.  
788 *Physical review Letters* 109.6 (2012).
- 789 [59] J. Engel Jr. “Outcome with respect to epileptic seizures.” *Surgical treatment of the epilepsies*  
790 (1993).
- 791 [60] A. Hillebrand et al. “Feasibility of clinical magnetoencephalography (MEG) functional mapping  
792 in the presence of dental artefacts”. *Clinical Neurophysiology* 124.1 (2013).
- 793 [61] S. Taulu and J. Simola. “Spatiotemporal signal space separation method for rejecting nearby  
794 interference in MEG measurements”. *Physics in Medicine & Biology* 51.7 (2006).

- 795 [62] S. Taulu and R. Hari. “Removal of magnetoencephalographic artifacts with temporal signal-space  
796 separation: demonstration with single-trial auditory-evoked responses”. *Human Brain Mapping*  
797 30.5 (2009).
- 798 [63] A. Hillebrand et al. “Frequency-dependent functional connectivity within resting-state networks:  
799 an atlas-based MEG beamformer solution”. *Neuroimage* 59.4 (2012).
- 800 [64] A. Hillebrand et al. “Direction of information flow in large-scale resting-state networks is frequency-  
801 dependent”. *Proceedings of the National Academy of Sciences* 113.14 (2016).
- 802 [65] L. Fan et al. “The human brainnetome atlas: a new brain atlas based on connectional architecture”.  
803 *Cerebral Cortex* 26.8 (2016).
- 804 [66] K. Sekihara et al. “Asymptotic SNR of scalar and vector minimum-variance beamformers for neu-  
805 romagnetic source reconstruction”. *IEEE Transactions on Biomedical Engineering* 51.10 (2004).
- 806 [67] D. Cheyne et al. “Event-related beamforming: a robust method for presurgical functional mapping  
807 using MEG”. *Clinical Neurophysiology* 118.8 (2007).
- 808 [68] M. Xia, J. Wang, and Y. He. “BrainNet Viewer: a network visualization tool for human brain  
809 connectomics”. *PLoS ONE* 8.7 (2013).
- 810 [69] *Brainwave*. <https://home.kpn.nl/stam7883/brainwave.html>.
- 811 [70] A. Bruns et al. “Amplitude envelope correlation detects coupling among incoherent brain signals”.  
812 *Neuroreport* 11.7 (2000).
- 813 [71] M. J. Brookes et al. “Measuring functional connectivity using MEG: methodology and comparison  
814 with fcMRI”. *Neuroimage* 56.3 (2011).
- 815 [72] J. F. Hipp et al. “Large-scale cortical correlation structure of spontaneous oscillatory activity”.  
816 *Nature Neuroscience* 15.6 (2012).
- 817 [73] G. L. Colclough et al. “How reliable are MEG resting-state connectivity metrics?” *Neuroimage*  
818 138 (2016).
- 819 [74] C. T. Briels et al. “In pursuit of a sensitive EEG functional connectivity outcome measure for  
820 clinical trials in Alzheimer’s disease”. *Clinical Neurophysiology* 131.1 (2020).
- 821 [75] P. Van Mieghem and K. Devriendt. “An epidemic perspective on the cut size in networks”. *Delft*  
822 *University of Technology, Report* 20180312 (2018).
- 823 [76] P. Van Mieghem. “Universality of the SIS prevalence in networks”. *arXiv preprint arXiv:1612.01386*  
824 (2016).
- 825 [77] S. Kirkpatrick, C. D. Gelatt, and M. P. Vecchi. “Optimization by simulated annealing”. *Science*  
826 220.4598 (1983).
- 827 [78] F. Wendling et al. “Computational models of epileptiform activity”. *Journal of Neuroscience*  
828 *Methods* 260 (2016).
- 829 [79] L. G. Kini et al. “Virtual resection predicts surgical outcome for drug-resistant epilepsy”. *Brain*  
830 142.12 (2019).
- 831 [80] M. Hashemi et al. “The Bayesian Virtual Epileptic Patient: A probabilistic framework designed  
832 to infer the spatial map of epileptogenicity in a personalized large-scale brain model of epilepsy  
833 spread”. *NeuroImage* (2020).
- 834 [81] J. Courtiol et al. “Dynamical Mechanisms of Interictal Resting-State Functional Connectivity  
835 in Epilepsy”. *Journal of Neuroscience* 40.29 (2020). Publisher: Society for Neuroscience Section:  
836 Research Articles.
- 837 [82] E. Cator and P. Van Mieghem. “Susceptible-infected-susceptible epidemics on the complete graph  
838 and the star graph: Exact analysis”. *Physical Review E* 87.1 (2013).
- 839 [83] U. T. Srinivasan et al. “Response of complex food webs to realistic extinction sequences”. *Ecology*  
840 88.3 (2007).

- 841 [84] J. P. Gleeson. “Cascades on correlated and modular random networks”. *Physical Review E* 77.4  
842 (2008).
- 843 [85] N. Masuda and P. Holme. “Predicting and controlling infectious disease epidemics using temporal  
844 networks”. *F1000prime reports* 5 (2013).
- 845 [86] O. E. Williams et al. “The shape of memory in temporal networks”. *arXiv preprint arXiv:2004.12784*  
846 (2020).
- 847 [87] P. Van Mieghem et al. “Influence of assortativity and degree-preserving rewiring on the spectra of  
848 networks”. *The European Physical Journal B* 76.4 (2010).
- 849 [88] B. Prasse and P. Van Mieghem. “Time-dependent solution of the NIMFA equations around the  
850 epidemic threshold”. *Journal of Mathematical Biology* 81.6 (2020).
- 851 [89] S. Olmi et al. “Controlling seizure propagation in large-scale brain networks”. *PLoS Computational*  
852 *Biology* 15.2 (2019).
- 853 [90] B. E. Youngerman and G. M. McKhann. “From Nodes to Networks: Can Virtual Resections  
854 Predict Neurosurgical Outcomes in Focal Epilepsy?” *Neurosurgery* 81.3 (2017). Publisher: Oxford  
855 Academic.
- 856 [91] V. K. Jirsa et al. “The virtual epileptic patient: individualized whole-brain models of epilepsy  
857 spread”. *Neuroimage* 145 (2017).
- 858 [92] M. Demuru et al. “Validation of virtual resection on intraoperative interictal data acquired during  
859 epilepsy surgery”. *Journal of Neural Engineering* 17.6 (2020).
- 860 [93] A. Holtmaat and K. Svoboda. “Experience-dependent structural synaptic plasticity in the mam-  
861 malian brain”. *Nature Reviews Neuroscience* 10.9 (2009).
- 862 [94] A. P. Millán et al. “Concurrence of form and function in developing networks and its role in  
863 synaptic pruning”. *Nature Communications* 9.1 (2018).
- 864 [95] C. J. Stam et al. “Emergence of modular structure in a large-scale brain network with interactions  
865 between dynamics and connectivity”. *Frontiers in Computational Neuroscience* 4 (2010).
- 866 [96] Y. Tao and B. Rapp. “Investigating the network consequences of focal brain lesions through  
867 comparisons of real and simulated lesions”. *Scientific Reports* 11.1 (2021).
- 868 [97] M. Yogarajah et al. “The structural plasticity of white matter networks following anterior temporal  
869 lobe resection”. *Brain* 133.8 (2010).
- 870 [98] J. Stretton et al. “Working memory network plasticity after anterior temporal lobe resection: a  
871 longitudinal functional magnetic resonance imaging study”. *Brain* 137.5 (2014).
- 872 [99] M. K. Sidhu et al. “Memory network plasticity after temporal lobe resection: a longitudinal func-  
873 tional imaging study”. *Brain* 139.2 (2016).